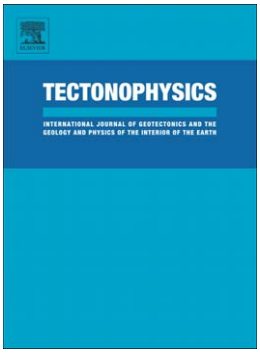

Evidence for the permo-triassic transtensional rifting in the iberian range (ne spain) according to magnetic fabrics results

C. García-Lasanta, B. Oliva-Urcia, T. Román-Berdiel, A.M. Casas, I. Gil-Peña, Y. Sánchez-Moya, A. Sopeña, A.M. Hirt, M. Mattei

PII: S0040-1951(15)00207-3
DOI: doi: 10.1016/j.tecto.2015.03.023
Reference: TECTO 126595

To appear in: *Tectonophysics*

Received date: 4 September 2014
Revised date: 16 March 2015
Accepted date: 28 March 2015

Please cite this article as: García-Lasanta, C., Oliva-Urcia, B., Román-Berdiel, T., Casas, A.M., Gil-Peña, I., Sánchez-Moya, Y., Sopeña, A., Hirt, A.M., Mattei, M., Evidence for the permo-triassic transtensional rifting in the iberian range (ne spain) according to magnetic fabrics results, *Tectonophysics* (2015), doi: 10.1016/j.tecto.2015.03.023

EVIDENCE FOR THE PERMO-TRIASSIC TRANSTENSIONAL RIFTING IN THE IBERIAN RANGE (NE SPAIN) ACCORDING TO MAGNETIC FABRICS RESULTS

C. García-Lasanta[a,*], B. Oliva-Urcia[b], T. Román-Berdiel[a], A. M. Casas[a], I. Gil-Peña[c], Y. Sánchez-Moya[d], A. Sopeña[d], A. M. Hirt[e] and M. Mattei[f]

[a] Departamento de Ciencias de la Tierra, Universidad de Zaragoza. Pedro Cerbuna 12, 50009 Zaragoza, Spain.

[b] Departamento de Geología y Geoquímica, Universidad Autónoma de Madrid. Francisco Tomás y Valiente 7, 28049 Madrid, Spain.

[c] Instituto Geológico y Minero de España. Ríos Rosas 23, 28003, Madrid, Spain.

[d] Instituto de Geociencias, UCM-CSIC. José Antonio Nováis 2, 28040, Madrid, Spain.

[e] Insitute of Geophysics, ETH-Zurich. Sonneggstrasse 5, 8092 Zurich, Switzerland.

[f] Dipartimento di Scienze, Università di Roma Tre. Largo San Leonardo Murialdo, 00146 Roma, Italy.

*Corresponding author: Tel.: +34 976762127 Fax: +34 976761106

E-mail addresses: lasanta@unizar.es (C. García-Lasanta), belen.oliva@uam.es (B. Oliva-Urcia), mtdjrb@unizar.es (T. Román-Berdiel), acasas@unizar.es (A. M Casas), i.gil@igme.es (I. Gil-Peña), yol@geo.ucm.es (Y. Sánchez-Moya), sopena@geo.ucm.es (A. Sopeña), ann.hirt@erdw.ethz.ch (A. M. Hirt), mattei@uniroma3.it (M. Mattei).

Abstract

Anisotropy of magnetic susceptibility (AMS) techniques are applied to Permo-Triassic red beds from the Castilian Branch (Iberian Range, NE Spain) that were deposited in an extensional basin inverted during Cenozoic times. The main goal of this work is to characterize the tectonic evolution of the basinal stage by differentiating synsedimentary to early diagenetic magnetic fabrics from the secondary tectonic fabrics related to compression, which are scarcely developed because no penetrative structures related to compression have been recognized. Oblate magnetic fabrics, with k_{min} axes perpendicular to bedding ,are observed in most cases. Magnetic lineations are variable, showing a dominant ENE-WSW maximum, which fits with a dextral transtensional regime acting on NW-SE master faults during the Triassic. We propose that variations

in the orientation of the magnetic lineation are associated with transfer faults which fragment the basin and trigger strain partitioning in different areas. Magnetic fabrics are locally modified by Cenozoic compression, with intermediate and minimum axes distributed along girdles perpendicular to fold axes. Comparing all these results with macrostructures and mesostructural kinematic indicators, we conclude that the fine-grained hematite-bearing rocks carry a consistent magnetic fabric which can be used to reconstruct the basin history.

Key-words: AMS, Castilian Branch, Permo-Triassic basin, red beds, magnetic mineralogy, transtensional regime.

1. Introduction

The origin of the Permo-Triassic Iberian Rift, which has been extensively studied, is related to the initial break-up of central Pangea (Alvaro et al., 1979; Sopeña et al., 1988; Arche and López-Gómez, 1996; Sánchez-Moya and Sopeña, 2004 and references therein). However, the complicated tectonic frame of this rifting stage, linked both to the opening and westward spreading of the Tethys and to the opening of the North Atlantic, remains a matter of debate. Furthermore, kinematic indicators at outcrop scale (e.g. fault striations, tension gashes) are scarce because of the detrital nature of the most abundant rocks. Therefore, they do not lead themselves in the reconstruction of the tectonic evolution of the sedimentary basin. In this frame, AMS analyses can help to unravel the tectonic development during the opening of the Permo-Triassic Iberian Rift.

Anisotropy of magnetic susceptibility (AMS) is a quick and non-destructive technique that allows analyzing the fabric of rocks. Provided that the magnetic mineralogy can be precisely determined, AMS has been demonstrated to be a marker of deformation. Careful control is necessary because AMS can be influenced by early sedimentary or diagenetic processes that can possibly lead to a partial overprint of the primary magnetic fabric, e.g., gravitational movements (Lowrie and Hirt, 1987; Pueyo Anchuela et al., 2011), paleocurrents

(e.g. Rees, 1965; Piper et al., 1996; Pueyo-Anchuela et al., 2013), or differential compaction processes (García-Lasanta et al., 2013b). The tectonic regime acting during the first stages of diagenesis has a first-order influence on the magnetic fabrics (e.g. Graham, 1966; Kissel et al., 1986; Mattei et al., 1997, 1999; Winkler et al., 1997; Sagnotti et al., 1998, 1999; Borradaile and Jackson, 2004; Cifelli et al., 2005; Oliva-Urcia et al., 2010a; Larrasoaña et al., 2004, 2011; Moussaid, et al., 2013; García-Lasanta et al., 2014); therefore, AMS is a key technique to unravel tectonic history of sedimentary basins. Under an extensional regime, magnetic lineation (k_{max} orientation) is commonly parallel to the extension direction and thus, perpendicular to the main normal faults (Mattei et al., 1997; Cifelli et al., 2005). On the contrary, in compressive contexts, magnetic lineation is oriented parallel to the strike of thrusts and perpendicular to the transport direction (e.g. Borradaile and Jackson, 2004), except in particular cases when shear deformation is associated with thrust sheets and a mixture of magnetic susceptibility carriers (Oliva-Urcia et al., 2009; Frizon de Lamotte, 2002). Deformational processes due to subsequent tectonic stages may occasionally mask or even completely modify the primary fabric, whereby the degree of this distortion is related directly to the amount of the subsequent deformation and its P-T conditions (Mattei et al., 1997; Parés et al., 1999; Soto et al., 2007, 2008; Oliva-Urcia et al., 2013).

We present the results of AMS recorded in red beds from a Triassic extensional basin that was subsequently inverted during the Cenozoic, in which no associated penetrative structures (i.e. cleavage) are observed. Transpressional deformation during inversion resulted in weakly deformed strata with shallow dips forming gentle folds, except in the vicinity of the main inverted faults. The principal aim of this work is to characterize the tectonic frame of Permo-Triassic rifting in the Castilian Branch through the study of the origin of the magnetic fabric, and determine its relationship with the sedimentary processes and the tectonic regimes acting during the basinal stage.

2. Geological setting

The Castilian Branch is a NW-SE structural alignment located in the southwestern part of the Iberian Range (NE Spain, Fig. 1A). This study focuses on its northwestern part (Fig. 1B), which is limited by the Central System (an asymmetric NE-SW upper crustal uplift formed by basement stacked thrusts, e.g. De Vicente et al., 2007; De Vicente and Vegas, 2009) towards the southwest, and the Almazán Cenozoic foreland basin to the northeast (Casas et al., 2000). The evolution of the whole Iberian Basin during the Permian and Mesozoic has been characterized by several extensional pulses (e.g. Salas and Casas, 1993; Ramos et al., 1996; Van Wees, et al., 1998), whose timing and magnitude are well constrained throughout the Iberian history (Salas and Casas, 1993; De Vicente et al., 2009).

The Castilian Branch developed as a rift basin during two of the main rifting stages, Permian and Triassic in age, as a response to lithospheric stretching (e. g. Alvaro et al., 1979; Sopeña et al., 1988; Arche and López-Gómez, 1996; Sánchez-Moya et al., 2004; De Vicente et al., 2009), and probably linked to the initial break-up of central Pangea (Sopeña and Sánchez-Moya, 1997). The rift trend was NW-SE, being controlled by previous faults that were active during Late Carboniferous-Early Permian (Sopeña et al., 1988; Arche and López-Gómez, 1996; Van Wees et al., 1998; Vargas et al., 2009). The most relevant structure of this type is the Somolinos Fault, which acted as the rift boundary towards the SW (Sopeña, 1979, Sánchez-Moya et al., 1996; Fig. 1B, C and D). Extensional displacements were distributed into several parallel NW-SE oriented faults (De Vicente et al., 2009; Fig. 1C), which were slightly oblique to the main boundaries of the Iberian microplate. Therefore, the entire Castilian Branch developed as a dextral strike-slip fault system in the inner part of the plate probably under a generalized ENE-WSW extension regime (De Vicente and Vegas, 2007; De Vicente et al., 2009).

Syn-rift Permo-Triassic red beds accumulated in half-grabens, lying unconformably on the Hercynian basement. They developed strong thickness variations related to their position within the trough-and-high systems in the

basin, and to trend variations along the master faults planes (e.g. Sopeña, 1979; Ramos et al., 1986; Sopeña and Sánchez-Moya, 1997; Sánchez-Moya and Sopeña, 2004; Vargas et al., 2009; Fig. 1C and D). Outcrop data indicate that Permian deposits reach thicknesses around 1500 m in some places (Hernando, 1977; Pérez Mazario et al., 1990; Sopeña and Sánchez-Moya, 2004), the highest along the whole Iberian Range. The Buntsandstein facies recorded four major vertical changes that can be explained by tectonics, climate change, variation in the sea level and other intrabasinal factors, but mostly due to intense subsidence variations (Sopeña and Sánchez-Moya, 1997; De Vicente et al., 2009). Amalgamated gravels and finer sandstones, both related to braided systems, were deposited during the two first stages. Widely spanned deposits followed, related to more evolved longitudinal fluvial systems, reaching the top of the Buntsandstein facies. Increased faulting influenced this episode, which was probably associated to the first Tethys transgression in the Triassic, when a renovated wide fluvial basin developed in the central and northeastern areas. Thickness of the Lower Triassic deposits varies from 60-80 m in the footwall of the Somolinos fault, to more than 850 m in the depocentres of the half grabens. The average thickness of outcropped Buntsandstein facies is around 250 m along the hanging wall (e. g. Sánchez-Moya and Sopeña, 2004). Continental conditions controlled the whole sedimentation processes during Late Permian-Early Triassic, until the Middle Triassic, when a deceleration in ttectonic activity occurred and the Tethys transgressed over a large part of Europe in response to mainly eustatic factors (Sopeña et al., 1988). This culminated in the deposition of shallow carbonate ramps (i.e. Muschelkalk facies) throughout the Iberian Range (e.g. Sánchez-Moya, 1992; Fig. 1C). After the Middle Triassic, subsidence continued at a constant rate and sedimentation of the transitional Keuper facies occurred (Sánchez Moya et al., 1992; Sopeña and Sánchez-Moya, 1997). They were deposited in relation to sabkha and paralic environments throughout the Iberian basin. Characteristically for the studied sector, the Keuper facies is essentially made up of red mudstones and detrital facies (alluvial to fluvial deposits and playa facies mainly consisting on fine grained sandstones, Muñoz Recio, 1993; Razola Mariño, 2011), with the

minor presence of evaporites, in contrast to other areas in the Iberian basin. Subsequently, Jurassic and Upper Cretaceous deposits unconformably covered the Triassic sediments with varied thickness of a few hundreds of meters on average, related to alternating transgression and regression episodes (Alvaro et al., 1979). Thicknesses of these units in the Castilian Branch are reduced when compared to the same units in other parts of the Iberian Range (De Vicente and Vegas, 2009).

NNE-SSW shortening of the whole Iberian Range led to a tectonic inversion during the Paleogene (Guimerà et al., 2004). In the Castilian Branch, this inversion was controlled by earlier NW-SE faults (Fig. 1C), and was therefore linked to a strong strike-slip component, which gave rise to a partial, oblique inversion of the Mesozoic basin (De Vicente and Vegas, 2009). Compressive structures trending NW-SE, are interpreted as gentle, forced folds linked to fault planes that usually root in Triassic faults and involve the Paleozoic basement (De Vicente et al., 2009). Tertiary shortening was mostly distributed within the area in short NE-SW trending folds with intermediate to steeply-dipping front limbs, probably linked to faults nucleated in the accommodation and relay ramps of the previous Triassic rifting system (De Vicente et al., 2009). These structures lead to a division of the region into sectors according to their trends and geographic position (Fig. 1B).

3. Methodology

To illustrate the tectonic characteristics of the Castilian Branch and to provide the AMS results with local structural information, detailed analyses of brittle mesostructures were made (Fig. 2) and examined in cross section on a regional level (Fig. 3). The three long cross sections are oriented from NW-SE to N-S, i.e. parallel or oblique to the main rifting trend (NW-SE) and perpendicular to the NE-SW compressive structures that are supposed to accommodate most of the Cenozoic shortening (De Vicente et al., 2009). Structural analyses are based on three main types of brittle structures, most of them located in the Buntsandstein sandstones: i) tension gashes, generally of milimetric opening rates and infilled

with quartz (Fig. 2C, I and J); ii) tensional or shear joints, arranged in perpendicular or conjugate sets (Fig. 2C and F), whose strikes can be represented in rose diagrams; and iii) decimetric to metric normal fault planes, generally disposed as conjugate sets with very small offsets (centimeters to one meter in exceptional cases, Fig. 2D, E and H) and, in some cases, slickenside striations (Fig. 2G). In faults with no striations strike and dip were measured, and it was possible to define the sense of displacement from stratigraphic markers or secondary structures in some of them (mainly R and R' fractures or intersection relationships).

The AMS sampling strategy was based on numerous previous works that describe the tectonic evolution of the Permo-Triassic rifting stage deposits by determining their lithology, origin and age (e.g. Hernando, 1977; Sopeña, 1979; Matesanz, 1987; García-Gil, 1989; Sánchez-Moya, 1992; Arche and López-Gómez, 1996; Sopeña and Sánchez-Moya, 1997; Díez et al., 2005; De Vicente and Vegas, 2009; De Vicente et al., 2009; Razola Mariño, 2011 and references therein). These investigations have provided a strict control over variables related to conditions in the sedimentary environment or lithological features. For this reason we only focus on sampling relatively homogeneous rock types so that we can isolate the tectonic influence on the magnetic fabric.

A total of 55 sites were collected in Permian (3 sites), Buntsandstein (38 sites), Muschelkalk (7 sites) and Keuper (7 sites) facies. The outcrops are located in gentle anticlines cored by Permo-Triassic rocks that have different trends and are separated by Lower Jurassic outcrops (Fig. 2A). The sampling strategy focused on red beds, mostly mudstones, siltstones and marls, in which flocculation was the depositional mechanism. Standard cylindrical paleomagnetic samples (25x21 mm), with an average of 10 samples per site, were obtained with portable gas- and electric drills.

3.1. Determination of magnetic susceptibility carriers

AMS studies require a careful determination of the magnetic phases present in the studied rocks and their influence on fabric orientation (Borradaile, 1988; Tarling and Hrouda, 1993; Lanza and Meloni, 2006, Hirt and Almqvist, 2012). In

order to address these issues, we need to characterize the present magnetic mineralogies and their relative contribution to the bulk AMS by applying different rock-magnetic techniques.

3.1.1. Thermomagnetic curves

We performed 25 temperature-dependent susceptibility curves (κ-T curves) using a KLY-3S susceptometer coupled with a CS3 furnace (AGICO Inc, Czech Republic) in the Laboratory of Magnetic Fabrics of the University of Zaragoza (Spain). The equipment records susceptibility while heating from 40ºC to 700ºC and cooling back to 40ºC in powdered samples of around 20-30mg in weight. The whole process is carried out in argon atmosphere, which avoids strong mineral oxidations during the heating process. In addition, empty furnace corrections are applied for all datasets. Heating-cooling runs allow checking the reversibility of curves and therefore the stability of the magnetic phases. The shape of the heating run gives information about the magnetic carriers. A hyperbolic shape in the initial part of the curves is typical when paramagnetic minerals are the main contributors to the magnetic susceptibility while a linear trend with a slight positive slope is typical of ferromagnetic phases (Hrouda et al., 1997). According to the method proposed by these authors, susceptibility can be divided into the paramagnetic (k_p) and ferromagnetic (k_f) components. When ferromagnetic phases are present, sharp decreases in susceptibility usually occur, related to the transition from ferromagnetic *s.l.* to paramagnetic behavior of a specific mineral (Hrouda, 1994), Curie temperature for magnetite (580ºC) or Néel temperature for hematite (680ºC). Data processing was developed with Cureval 8.0 software (Chadima and Hrouda, 2009).

3.1.2. Remanent magnetization procedures

Lithological characteristics of the red beds sampled in this study suggest a significant content of ferromagnetic *s.l.* phases that may influence the magnetic fabric. Neoformation of new ferromagnetic phases during heating can take place, altering the original content. For this reason, classical remanent magnetization measurements were carried out, combining different magnitude of magnetic fields and thermal demagnetization procedures. These analyses

were performed at the Paleomagnetism Laboratory of Roma Tre University (Rome, Italy).

Acquisition curves of isothermal remanent magnetization (IRM) refer to the remanent magnetization acquired for a sample when applying stepwise increasing DC magnetic fields. The shape of the acquisition curve provides information about the coercivity of the magnetic minerals (Dunlop, 1972). IRM curves were obtained on 14 selected samples, which represent the range of lithologies examined in this study. An ASC pulse magnetizer (ASC Scientific, USA) was used to generate magnetic fields in 31 steps starting from the NRM (natural remanent magnetization) value to a maximum field increased in 2000 mT. Magnetic remanence was measured with an automatic JR6 spinner magnetometer (AGICO Inc, Czech Republic). Acquired data were analyzed with the IRM-CLG 1.0 worksheet (Kruiver et al., 2001), which allows a statistical analysis of the contribution to the total IRM acquisition curve of each mineral phase with respect to their mean coercivities. Backfield procedure was applied to the same samples, by stepwise increasing magnetic fields in the opposite direction using a total of 20 increments. The magnitude of the magnetic backfield needed to remove the original IRM is the coercivity of remanence, and is diagnostic for grain-sizes differentiation in ferromagnetic phases (Day et al., 1977).

These analyses were complemented by a thermal demagnetization of a cross-component IRM (Lowrie, 1990). Three decreasing magnetic fields (2000, 600 and 120mT in our case) were applied to each sample with the ASC pulse magnetometer in three orthogonal positions (z, y and x, respectively). Therefore, minerals were remagnetized and oriented according to their coercivity. Subsequently, samples were thermally demagnetized stepwise, by heating them in a zero-field with an ASC TD48 oven (ASC Scientific, USA) from room temperature to 680ºC. Remanent magnetization was measured for each step on the JR6 spinner magnetometer.

3.2. AMS techniques

Low-field AMS, which is measured at room temperature (LF-AMS at RT), provides the magnetic fabric orientation for the whole rock, that results from the sum of contributions from each of the magnetic phases. In addition to the applied methods for magnetic minerals recognition, we applied different techniques of AMS measurement that allow isolating the contribution of the ferro- and paramagnetic phases. This allowed us to check for possible differences in orientation for each subfabric.

3.2.1. Low-field AMS at room temperature (RT)

LF-AMS at RT was measured in 810 specimens from 55 sites located along Permo-Triassic outcrops (mainly from the Lower Triassic) of the western part of the Castilian Branch. AMS was analyzed with a KLY3 Kappabridge (AGICO, Czech Republic) susceptometer at the University of Zaragoza. This set of data was briefly discussed in García-Lasanta et al. (2013a). The AMS ellipsoid, with principal axes $k_{max} \geq k_{int} \geq k_{min}$, can be used to describe the ellipsoid geometry and its degree of anisotropy. These two can be quantified by, respectively, the shape parameter, T, and the corrected anisotropy degree, P_j (Jelinek, 1981):

$$T = \frac{2\mu_2 - \mu_1 - \mu_3}{\mu_1 - \mu_3} \qquad Pj = \exp\sqrt{2\left[(\mu_1 - \mu_m)^2 + (\mu_2 - \mu_m)^2 + (\mu_3 - \mu_m)^2\right]}$$

where μ_1, μ_2 and μ_3 represent $\ln(k_{max})$, $\ln(k_{int})$ and $\ln(k_{min})$, respectively, and $\mu_m = (\mu_1 + \mu_2 + \mu_3)/3$. Magnetic lineation L ($k_{max}/k_{int}$) and magnetic foliation, F (k_{int}/k_{min}) are also used to complement the characterization of the magnetic ellipsoids. Data processing was carried out with the Anisoft 4.2 software (Chadima and Jelinek, 2009).

3.2.2. Low-field AMS at low temperature (LT)

LF-AMS at LT measurements exploit the fact that the paramagnetic susceptibility of a rock is exponentially enhanced at low temperatures, according to the Curie-Weiss law: $k_{para} = C/T-\Theta$, where k_{para} is the paramagnetic susceptibility, C the Curie constant, T the temperature, and Θ the paramagnetic Curie temperature (e.g. Ihmlé et al, 1989; Ritcher and Van der Plujim, 1994;

Dunlop and Özdemir, 1997; Parés and Van der Pluijm, 2002; Biedermann et al., 2014). When measuring a purely paramagnetic phase at around 77K, the ratio between the low temperature and the room temperature susceptibility is around 3.8 (Ritcher and van der Plujim, 1994; Lüneburg et al., 1999). The presence of ferromagnetic *s.l.* minerals decreases this ratio (Oliva-Urcia et al., 2010a). This technique gives repeatable results (Hirt and Gehring, 1991; Lüneburg et al., 1999; Oliva-Urcia, et al., 2010a, 2010b). Therefore, susceptibility measurements at low temperature will mainly reflect the paramagnetic subfabric when the ratio of the susceptibility measured at low temperature respect to the room temperature is close to 3.8, although values higher than 2 in marls are considered significant (Oliva-Urcia et al., 2010a, 2010b, 2013). The analyses were performed at the University of Zaragoza on 35 standard samples from 5 sites in a KLY-3S Kappabridge (AGICO, Czech Republic). The samples were immersed in a dewar filled with liquid nitrogen for 30-40 minutes before starting the measurements, in order to acquire a homogeneous temperature of 77K, and again around 10 minutes more between each of the three spinner positions required by the apparatus procedure.

3.2.3. High-field AMS at room temperature

The high-field AMS (HF-AMS) at room temperature method allows extracting the ferrimagnetic signal (i.e., magnetite, pyrrhotite) and the dia-/paramagnetic components from the total AMS in standard samples (Richter and Van der Pluijm, 1994; Martín-Hernández and Hirt, 2001, 2004; Martín-Hernández, 2002; Martín-Hernández and Ferré, 2007). Problems can arise when high-coercivity ferromagnetic minerals are the main susceptibility carriers.

HF-AMS at room temperature was performed using a torque magnetometer from the Laboratory of Natural Magnetism at the ETH (Zurich, Switzerland). The analyses of 20 standard paleomagnetic cores (cylinders of about 10.3 cm^3) from four different sites was measured for seven magnetic fields in three orthogonal positions: 0mT (no external field), 1000mT, 1100mT, 1200mT, 1300mT, 1400mT and 1500mT and corrected for zero-field and holder signals (e.g. Martín-Hernández and Hirt, 2004; Schmidt et al., 2007; Almqvist, et al., 2011).

4. Results

4.1. Cross sections and structural analyses

An overview of the three cross sections (Fig. 3) corroborates the low imprint of compressional deformation and the dominance of gentle asymmetric folds oriented NE-SW. These folds are related in most cases to steeply-dipping reverse faults in their (usually southern) front limbs. These faults show displacements that are generally smaller than 100m, although some exceptions are found (Fig. 3, cross section II-II'). The detailed cartography (Fig. 2A) indicates that most structures involving the Paleozoic and its Lower Triassic cover are gentler toward the Jurassic-Cretaceous sequence (Fig. 3, I'-I'', II-II', III-III'), which could probably detach at the Upper Triassic shales (and evaporites). Only the largest faults would deviate from this pattern and remain constant along the whole Mesozoic cover.

Cross sections also illustrate the minor thickness variations of the Lower Triassic units along a NW-SE direction, corroborating that sedimentation during the rifting process was preferentially controlled by several parallel NW-SE oriented faults (De Vicente et al., 2009) and remarkable thicknes changes occurred along that direction. Only a slight reduction of thickness towards the W has been reported by previous works (e.g. Sánchez-Moya, 1992). Both changes in thickness of the Triassic units and the geometry of folds point to a thick-skinned deformational style, involving at least the upper units of the Palaeozoic basement (Fig. 3).

Only brittle mesostructures can be observed on an outcrop scale in the Lower and Middle Triassic units. Cleavage is absent even in fine-grained rocks in the vicinity of faults. Brittle mesostructures have been studied in a total of 24 outcrops along the area (Fig. 2). They show relatively heterogeneous orientation patterns, related either with extensional or compressional stages. In some cases, when no sedimentary or structural criteria (e.g. sedimentary thickness changes) are available, it is difficult to determine the age of the structures. The partial coaxiallity between extensional and inversion stages also

contributes to this problem. In this sense, AMS is a powerful resource to unravel deformational history in this type of tectonic settings. All in all, some general characteristics can be described for the different types of analyzed structures.

In sites in which fault planes were detected, they usually strike NW-SE and are arranged in two conjugate sets, defining Andersonian systems (e.g. Fig. 2D, E, RC22a in G and H). Small throws, from several centimeters to several decimeters, are observed and support normal fault movement. The extension direction deduced from a simple analysis of these systems is in general NE-SW, but some exceptions are observed, from N-S (RC20 in Fig. 2) to NW-SE (RC14 in Fig. 2), with examples in which orientation patterns are almost radial (RC41 in Fig. 2). Striae were clearly detected only in one site, in which their geometric arrangement indicates a reactivation of the normal fault planes by a strike-slip event (RC22b in Fig. 2G). In general, all these conjugate systems can be interpreted as pre-folding since two of the stress axes are contained within the bedding plane.

Tension gashes of different scales have also been observed in several outcrops. They are infilled with quartz in the Buntsandstein sandstones (Fig. 2C and I) and with carbonates in the Muschelkalk limestones (Fig. 2J). Their length varies at each outcrop and when shorter they usually define *en échelon* arrays, with most of the gashes oriented NNW-SSE. If considered pure extensional, the poles to their trends mark the extension direction in which they generated that varies from NNE-SSW (RC13 in Fig. 2) to ENE-WSW (RC28 in Fig. 2). In one site (RC22a in Fig. 2G) several tension gashes are oriented parallel to normal fault planes that do not show striae. On the contrary, no tension gashes parallel to the two sets of reactivated faults have been detected.

Systems of joints are the third type of analyzed brittle structures. From rose diagrams, two sets are generally found at each site (e.g. Fig. 2G), one is usually more pervasive and cuts its conjugate set (Fig. 2B). Some of the joint systems may correspond to conjugate shear joints, whereas orthogonal sets may correspond to tensional joints, because of their correspondence with orientation

of other structures. The principal sets observed in different outcrops show orientations from NE-SW to NNW-SSE.

4.2. Magnetic carriers

For the 810 specimens analyzed, bulk susceptibility values range between 29.05 and 397.9x10^{-6}SI, with values between 50 and 300x10^{-6}SI for 96.4% of the samples (Fig. 4). The 25 thermomagnetic curves corroborate the presence of a ferromagnetic *s.l.* mineral (Fig. 5). In 18 cases, the hyperbolic shape in the first segments of the curves (Fig. 5A and B) demonstrates that a wide paramagnetic fraction accompanies the ferromagnetic *s.l.* phase. This paramagnetic susceptibility is most likely associated with phyllosilicate minerals.

The unblocking behavior in 20 of the 25 samples display a decay in the heating run at the Néel temperature of hematite (Fig. 5A to D). Eight out of these 20 samples show reversibility between heating and cooling runs, indicating a stable phase and no mineral neoformation during heating (Fig. 5D). In the other cases, neoformation of magnetite takes place, as seen in the cooling curves (Fig. 5A and C). The other five heating curves show two decays, firstly a subtle one at the Curie temperature of magnetite, and subsequently a major one, coinciding with the Néel temperature of hematite (Fig. 5E).

In 17 samples the presence of pure hematite is corroborated by the susceptibility decay, which occurs in a narrow temperature range around 670-680ºC (Fig. 5A to C and E), which sometimes displays a Hopkinson peak (e. g. Fig. 5C). In the other 8 cases, the susceptibility decay occurs between 620 and 640ºC (always above 600ºC) (Fig 5D), indicating grain size effects or the possible presence of other magnetic phases as maghemite or impurities (Soto et al., 2012). Because there was some ambiguity in interpreting the thermomagnetic curves, further rock magnetic tests were applied.

IRM acquisition curves show in some cases a concave-upward curve in their initial part, which is diagnostic of the lack of low-coercivity phases (Fig. 6A, sample RO4-1A, Martín-Hernández and Hirt, 2004). The magnetization is not completely saturated at 2T, which is indicative for a high coercivity phase (Fig.

6A). This phase is confirmed when applying the procedure of Kruiver et al. (2001), whereby 82 and 99% of the total IRM is carried by a mineral with mean coercivity between 355 and 934mT (Fig. 6B). The remainder of the IRM can be attributed to a second phase (between 1 and 18%) with a mean coercivity between 28 and 141mT. Remanent coercivity is approximately between 325 and 885mT (Fig. 6A), and there is a direct correlation between the highest of these values and the highest mean coercivities.

Results from the thermal demagnetization of a composite IRM show high magnetization values in the axes where the high and intermediate fields were applied and a negligible magnetization where we applied the lower field. This confirms that the low-coercivity minerals (e. g. magnetite, maghemite, Fig. 6C) have only a small contribution to the total magnetization. When thermally demagnetizing the samples, a sharp decrease in magnetization is observed between 590 and 680ºC for the high and intermediate axes.

4.3. Low field magnetic fabrics at room temperature

The average scalar parameters are shown per site in Table 1 and in Fig. 7. Bulk susceptibility values range between 52.1×10^{-6}SI in site SI7 and 296×10^{-6}SI at site CO2. Average values of the corrected anisotropy degree range between 1.014 and 1.087 (AL2 and AL6, respectively). Only site RE6 exceeds this range, reaching a Pj value of 1.137. The shape parameter T is positive at all sites (between 0.09 for site RO1 and 0.949 for site SI1), indicative of a prevalent oblate shape for all the AMS ellipsoids. Magnetic lineation parameter varies from 1.001 to 1.013, while magnetic foliation ranges between 1.010 and 1.070, except in site RE6, where F reaches a value of 1.113. There is a weak positive correlation between Pj and k_m (Fig. 7A) and between Pj and T (Fig. 7B).

The principal axes of the AMS ellipsoid display two types of fabrics (Table 2): i) 46 sites show k_{min} axes clustered around the pole to the bedding plane (Fig. 8A to E), and ii) 9 sites (Figs. 8G, H and 9) show k_{min} and k_{int} axes distributed within a girdle, clearly developed in five cases and more incipient in the other four. In the first group, magnetic lineations show diverse degrees of scattering, from radial distributions (Fig. 8A) to more clustered patterns, with two

main perpendicular maxima NW-SE and NE-SW (Fig 8B and C, respectively) and two secondary, N-S and E-W (Fig 8D and E, respectively). Sites RE6, RS1 and RS9 are special cases, because magnetic lineation appears scattered along two directions in the same site (Figs. 8F and 9). In the second group, magnetic lineation is generally more scattered than in the first group, and is oriented NE-SW in five cases (four of them corresponding to well developed girdles Fig. 8G) and NW-SE in the other four (Fig. 8H).

The variability in the orientations of magnetic lineations can be better understood considering their location within the structural frame of the Castilian Branch. To help in the visualization, rose and density diagrams are shown in Fig. 9, comprising all the samples measured in each sector. Resuts from these sites can be summarized: 1) Retortillo de Soria (RE) shows a general distribution of the k_{max} axes that is radial but an additional ENE-WSW maximum is observed; 2) Condemios (CO), the sector located in the footwall of the Somolinos NW-SE trending fault, shows a radial distribution; 3) Alpedroches (AL) from the hanging wall of the Somolinos fault is strongly variable with an ENE-WSW trending maximum; 4) Riba de Santiuste (RS) has a main maximum trending ENE-WSW and a secondary one oriented NE-SW; 5) Sigüenza (SI) displays a major NE-SW trending maximum and secondary NNW-SSE orientation; 6) Romanillos (RO), has a general E-W trend; 7) Yelo (YE) shows an ENE-WSW maximum; and 8) Arcos de Jalón (AJ) has a NW-SE and N-S maxima.

4.4. Results from subfabrics separation methods

Low temperature AMS was measured at five sites and results are given in Table 3. Ratios of low temperature bulk magnetic susceptibility (k_m-LT) to room temperature bulk susceptibility (k_m-RT) are between 2.10 and 2.71. The ferromagnetic content deduced from the thermomagnetic curves is inversely proportional to k_m-LT/k_m-RT ratios, confirming the presence of a ferromagnetic phase. This increase, despite its low value, corroborates the presence of a paramagnetic, temperature-dependent signal. We observe the same orientation of the k_{min} axes at LT and RT in all cases (Fig. 10). The k_{max} and k_{int} axes are

more distributed in the foliation plane at LT compared to RT in 3 out of the 5 sites (Fig. 10A). This would be expected if the paramagnetic AMS arising from phyllosilicates is enhanced at LT. In summary, the mean orientation at site scale is the same under both temperature measurements in 4 of the 5 sites (Table 3).

The rock magnetic results indicate that hematite is the predominant ferromagnetic *s.l.* phase in these rocks. It should be noted that hematite will not be completely saturated in fields <1.5T, which are used to determine the high-field AMS. Therefore, results from the separation of the high-field AMS will be shown in general terms as saturated and non-saturated subfabrics. The percentage of non-saturated signal ranges between 56 and 77% in the 20 samples from four sites, and thus, saturated signal varies between 23 and 44%. Magnetic foliation planes of both saturated and non-saturated subfabrics are parallel to the bedding plane (Fig. 11). Magnetic lineation at low-field is parallel to the non-saturated subfabric in two cases (Fig. 11A). In the other two cases, magnetic lineation at low field is in an intermediate position between the two subfabrics obtained in the torque separation (Fig. 11B), but nearer to the saturated fraction. In any case, magnetic lineations found in high field are similarly or better grouped than measurements in low field.

5. Discussion

The main carriers of the magnetic susceptibility are paramagnetic minerals (probably represented by phyllosilicates of the matrix, Fig. 5A and B) and, to a lesser extent, hematite (high-coercivity component 1 in Fig 6B). Bulk magnetic susceptibilities seldomly exceed $300x10^{-6}$SI, what could correspond to the typical range of a main paramagnetic contribution (Rochette, 1987). However, since hematite can also carry a relatively low magnetic signal, results from additional procedures were essential to determine the relative contribution of both phases. Thermal demagnetizations of the composite IRM show a range of unblocking temperatures, between 590 and 680ºC, wider than in the thermomagnetic curves, where decays in susceptibility occur generally at 680ºC. This temperature range supports the presence of hematite that has

variations in grain size, stoichiometry or composition (Lattard et al., 2006). Magnetite is identified in several samples from thermomagnetic curves (Fig. 5E) and demagnetization of the composite IRM (Fig. 6C). However, the negligible magnetite content (low-coercivity component 2, Fig 6B) and the dominance of high coercivity hematite is supported by the coercivity analysis of IRM and its thermal unblocking.

Methods that isolated the AMS subfabrics have been useful in interpreting which minerals are responsible for the observed AMS (i.e. phyllosilicates and hematite). LF-AMS at 77K confirms that the paramagnetic minerals, whose magnetic fabric is enhanced at low temperature (e.g. Biedermann et al., 2014 and references therein), contribute to the total AMS. However, they also confirm that a ferromagnetic component influences the LF-AMS at room temperature, because the enhancement factor at 77K is lower than expected for purely paramagnetic samples. The orientation of the magnetic fabric is similar at both low and room temperatures, which suggests that the same processes control all minerals sub-fabrics. The only difference is that the k_{max} and k_{int} axes are more scattered at LT, which would be expected because phyllosilicates and hematite have a very oblate AMS (Martín-Hernández and Hirt, 2003).

High-field AMS is complicated by the lack of complete saturation of the hematite component, which cannot be isolated by the method outlined in Martín-Hernández and Hirt (2004). Therefore, it will contribute to the dia-/paramagnetic AMS (i.e. the unsaturated AMS). The presence of a ferromagnetic *s.l.* phase, which is not saturated after applying 1.5T, would lead to an overestimation of the paramagnetic content. Hematite has a strong AMS related to its crystalline structure, with the k_{min} along the crystallographic c-axis (Martín-Hernández and Hirt, 2004). However, we observe that the saturated and unsaturated components of the high-field AMS are both controlled by bedding compaction, since the magnetic foliation planes of both components are parallel to the bedding plane in all cases. The k_{max} axes orientation of the unsaturated fraction usually agrees with the LF-AMS at room temperature,

which suggests that the magnetic lineation arises from hematite and phyllosilicates.

The possible influence of paleocurrents on the orientation of magnetic fabrics should also be taken into consideration (e.g. Piper et al., 1996; Pueyo Anchuela et al., 2013). The studied red beds were deposited in fluvial environments during the Early Triassic, and affected by strong subsidence changes related to half-grabens. The possible influence of paleocurrents was minimized by focusing the sampling on fine-grained lithologies (claystones and siltstones). Flocculation processes govern clays deposition and therefore the effect of paleocurrents in the petrofabric is minimized. We also discarded the presence of paleocurrent-related sedimentary structures at outcrop scale and ensured a rigorous stratigraphic localization of our sites.

In summary, we can interpret that all our magnetic fabric results are only conditioned by the tectonic regime, from deposition through their complete diagenesis and exhumation history.

5.1. Tectonic implications of the magnetic fabric orientation

A slight positive correlation was observed between scalar parameters (Fig. 7), although it does not seem statistically significant. Nevertheless, previous correlations between scalar parameters trend (Pj-T) and strain would associate our range of values with a synsedimentary origin of the magnetic fabrics (Borradaile and Henry, 1997; Parés, 2004; Robion et al., 2007). The idea of a sedimentary origin is also supported by the orientation of the minimum axes at 46 sites, perpendicular or subperpendicular to the bedding plane. In nine out of these 46 sites, magnetic lineation is distributed in a radial pattern on the bedding plane, reinforcing the idea of a magnetic fabric linked only to compactional processes. In the other 37 sites where the k_{min} axes remain perpendicular to bedding, a different degree of clustering of the magnetic lineation is observed. As demonstrated in previous investigations, the orientation of the magnetic lineation can provide information about the tectonic processes contemporary or postdating sedimentation and compaction (e.g. Kissel et al., 1986; Mattei et al., 1997, 1999; Sagnotti et al., 1998, 1999;

Borradaile and Jackson, 2004; Cifelli et al., 2005; Larrasoaña et al., 2004; Soto et al., 2007, 2008; Oliva-Urcia et al., 2010a; Moussaid, et al., 2013; García-Lasanta et al., 2014). In the other nine out of 55 sites, the k_{int} and k_{min} axes are distributed within a girdle, which indicates incipient development of subsequent compressional fabrics that usually predates the formation of penetrative structures (Oliva-Urcia et al., 2013). According to several authors, this superimposed fabric could probably be carried by mineral phases neo-crystallized during the compressional stage (Oliva-Urcia et al., 2009; Frizon de Lamotte, 2002).

From the 46 sites where the k_{min} axes are oriented closely to the bedding pole, 34 are located in Permian and Early Triassic deposits infilling the half-grabens. Since no penetrative deformation is associated with Tertiary inversion, the observed magnetic lineations are interpreted as an early fabric related to the extensional synsedimentary context. A unified representation of these magnetic lineations, after bedding correction to the horizontal, shows a main ENE-WSW direction (Fig. 12A), that in general terms is interpreted as the main extension direction. The extensional origin of magnetic lineation is also supported by results from the 12 remaining sites from the upper units with similar lithology (red mudstones of the Middle and Upper Triassic, Muschelkalk and Keuper facies) that show vertical k_{min} axes after bedding correction. The k_{max} axes in these samples show a lower degree of clustering higher in the stratigraphic profile. A main ENE-WSW direction is preserved in the Middle Triassic deposits (Fig 12B) and evolves to a more radial pattern for the Upper Triassic sediments (Fig 12C). This change in the orientation of the magnetic lineations with time is consistent with the development of synsedimentary structures: Lower Triassic units show the more important syntectonic unconformities linked to NW-SE structures when the higher subsidence rates took place in the area, whereas thickness changes are more subtle in the Middle and Late Triassic units. Results also support a primary origin for the magnetic lineation, which is interpreted to be influenced by both sediment compaction and tectonic activity during the Early Triassic and only by sediment compaction towards the Late Triassic.

The primary origin for the magnetic fabric is also supported by results sharing the same time-span but different paleogeographical position with respect to the rift boundaries. Three out of the 34 sites from the Buntsandstein facies, which belong to sector 2 (CO in Figs. 1, 2 and 9), show magnetic lineations distributed in a radial pattern on the bedding plane (Fig. 9). This sector is located in the footwall of the rifting area (southwest to the Somolinos fault, Figs. 1, 2), where the smallest thickness (Sánchez-Moya, 1992) of syn-rift materials is found, and therefore, they are not affected by subsidence or extensional tectonics.

Data from structural analyses demonstrate the parallelism between magnetic lineation orientation and local extensional directions in several cases. The studied sets of tension gashes can be interpreted to be originated in relation to extension directions between NNE-SSW and ENE-WSW. When comparing these results with the specific AMS data at each site, we observe a clear parallelism between the extension direction given by the tension gashes and the magnetic lineation orientation (see e.g. sites RC13 RC28 and RC32 in Fig. 2 and sites RS1-RS2-RS3, SI3 and SI7 in Fig. 9, respectively). Site RC22a (Fig. 2G) presents a set of tension gashes, which suggests an extension direction parallel to the magnetic lineation at site SI4 (Fig. 9). In this case, two conjugate sets of normal faults striking sub-parallel to the tension gashes also indicate an extension direction parallel to the described magnetic lineation. Slickenfibers observed on a third set of fault planes probably originated by a strike-slip reactivation of previous normal fault planes and the stress direction compatible with striae is not related to the magnetic lineation orientation. This illustrates that the inversion processes had only a small influence on the primary magnetic fabric. Systems of conjugate fault planes recognized at other structural sites are consistent with extension directions parallel to the magnetic lineation obtained in their neighboring AMS sites (e.g. RC2-3-4-5 and AJ4, RC7 and RO2, Figs. 2 and 9, respectively). In some cases, structural results defined an extension direction near sites in which magnetic fabrics show the k_{max} axes scattered within the magnetic foliation plane (e.g. RC14 and RS1, RC20 and AL3, Figs. 2 and 9, respectively), indicating either a preferred extension

direction within a nearly radial extensional regime (Simón et al., 1988) or structural data collecting biased by outcrop orientation. Therefore, the most relevant extensional features obtained corroborate that the extensional regime influenced the orientation of the registered magnetic lineation.

In summary, the dominant magnetic lineation from the syn-rift deposits indicates a ENE-WSW extension direction, oblique to the two sets of major faults controlling basinal evolution in the Castilian Branch: a main set represented by the Somolinos fault, with approximately NW-SE orientation, and a probable secondary set, represented by faults interpreted to control the orientation of the basement-cored anticlines with NE-SW orientation. The main trend for the magnetic lineation is consistent with the dextral transtensive regime determined for the Triassic rifting in the Castilian Branch, controlled by faults oriented NW-SE (De Vicente et al., 2009, De Vicente and Vegas, 2009 and references therein). The combination of a dextral E-W shear with main NW-SE faults would give a main ENE-WSW stretching direction that could vary accordingly with the rate of divergence in the NNE-SSW direction.

Variability in the orientation of magnetic lineations, although moderate, when present, can explained with respect to the geographic distribution of sites and their particular position with respect to structural features (Fig. 13). These variations, when significant, seem directly related to the direction of the major structures close to each site. In sector 1 (RE Fig. 9) ENE-WSW trending lineations are dominant in general, whereas the westernmost area shows WNW-ESE lineations, parallel to the outcrop trend in the sector, which is controlled by the Somolinos fault. Sector 4 (RS in Fig. 9), located in the central part of the basin, shows magnetic lineations with a general ENE-WSW trend. However, a secondary maximum with NE-SW direction can be observed, indicating a lower influence of strike-slip motion compared to pure extension for the central part of the basin. Sector 5 (SI in Fig. 9) shows dominantly ENE-WSW trending lineations, but also NW-SE trending lineations are observed, probably influenced by major NW-SE faults that control the following outcrops eastward (see Figs. 2 and 9).

The differences between regional and local patterns in the orientations of the magnetic lineation (Fig. 13) are therefore interpreted as an effect of strain partitioning controlled by the orientation of previous structures. Locally, the transtensional process was distributed into both purely extensional structures, i.e. faults bounding the subsequently inverted areas which formed the basement-cored anticlines with NE-SW trending axes, and strike-slip adjacent structures that are mainly the steeply-dipping, major NW-SE faults. On the other hand, the strain-partitioning pattern during Cenozoic transpression in the Castilian Branch (De Vicente et al., 2009) could also have been the cause of some variations in the magnetic fabrics, as observed from the girdled distributions of the k_{min} and k_{int} axes. Structural data from conjugate sets of joints and reactivated faults are generally consistent with an Andersonian model of a strike-slip regime. Thus they indicate NNE-SSW and NNW-SSE compression directions, perpendicular or oblique to the main basement-cored folds. These diverse compressional directions have been referred by previous authors in other areas of the Iberian Range (Liesa and Simón, 2009).

6. Conclusions

Magnetic fabrics applied to Triassic red beds in the Castilian Branch allow characterizing the deformation linked to early stages of basin evolution. Rock magnetic procedures distinguished two main contributors to the magnetic fabric, which are phyllosilicates and hematite. Magnetic subfabrics separation demonstrates that both phases share the same magnetic orientation and, therefore are used to isolate the tectonic signal in the orientation of the magnetic ellipsoid.

Sedimentation during the Early Triassic was controlled by the orientation of major faults limiting the rift (NW-SE). This process was recorded by the AMS in most of the sites, leading to the development of a magnetic lineation with an overall ENE-WSW trend, and showing different orientations depending on the location of sites with respect to the main rifting boundaries. These results fit with a dextral transtensional regime along an E-W shear corridor during the Late

Permian-Early Triassic for the development of the magnetic fabric. In other sites, the magnetic fabric maintained a typical sedimentary shape, with a radial distribution for the k_{max} axes scattered along the magnetic foliation plane. The Cenozoic tectonic inversion process did not produce penetrative deformational structures in the Triassic materials and modified the extensional magnetic fabric orientation only in a few sites.

7. Acknowledgments

The authors want to thank Gerardo de Vicente for his suggestions and ideas at the beginning of this work, Hans-Peter Hächler for his support in the process of torque measurements developed in the LNM at the ETH Zürich and Massimiliano Porreca for his advices during the measurements performed in Roma Tre. We also acknowledge the use of Servicio General de Apoyo a la Investigación-SAI, Universidad de Zaragoza (Servicio de Preparación de Rocas y Materiales Duros). The manuscript benefited greatly from thorough reviews by Jean-Phillipe Avouac, Dominique Frizon de Lamotte and an anonymous reviewer. This study was financed by the research project CGL2009-08969 of the MICINN (Spanish Ministry of Science and Innovation). C. García-Lasanta also acknowledges the MICINN for the research grant BES-2010-037509.

8. References

Almqvist, B. S. G., Hirt, A. M., Herwegh, M., Leiss, B., 2011. Magnetic anisotropy reveals Neogene tectonic overprint in highly strained carbonate mylonites from the Morcles nappe, Switzerland. Journal of Structural Geology 33, 1010-1022.

Álvaro, M., Capote, R., Vegas, R., 1979. Un modelo de evolución geotectónica para la Cadena Celtibérica. Acta Geológica Hispánica 14, 172-177.

Arche. A., López-Gómez, J., 1996. Origin of the Permian-Triassic Iberian Basin, central-eastern Spain. Tectonophysics 266, 443-464.

Biedermann, A. R., Koch C. B., W. E. A. Lorenz, A. M. Hirt, 2014. Low-temperature magnetic anisotropy in micas and chlorite. Tectonophysics, *in press.* doi: 10.1016/j.tecto.2014.01.015.

Borradaile, G. J., 1988. Magnetic susceptibility, petrofabrics and strain. Tectonophysics 156, 1-20.

Borradaile, G. J., Henry, B., 1997. Tectonic applications of magnetic susceptibility and its anisotropy. Earth-Sciences Reviews 42, 49-93.

Borradaile, G. J., Jackson, M., 2004. Anisotropy of magnetic susceptibility (AMS); magnetic petrofabrics of deformed rocks. Geological Society. Special Publication 238, 299-360.

Casas, A. M., Cortés, A. L., Maestro, A., 2000. Intra-plate deformation and basin formation during the Tertiary at the Northern Iberian Plate: origin and evolution of the Almazán basin. Tectonics 19, 762-786.

Chadima, M., Hrouda, F., 2009. Cureval 8.0: Thermomagnetic Curve Browser for Windows. Agico, Inc.

Chadima, M., Jelinek, V., 2009. Anisoft 4.2: Anisotropy Data Browser for Windows. Agico, Inc.

Cifelli, F., Mattei, M., Chadima, M., Hirt, A. M., Hansen, A., 2005. The origin of tectonic lineation in extensional basins: Combined neutron texture and magnetic analyses on “undeformed” clays. Earth Planet Science Letters 235, 62-78.

Day, R., Fuller, M., Schmidt, V. A., 1977. Hysteresis properties of titanomagnetites: Grain size and composition dependence. Phys. Earth Planet. Inter. 13, 260-267.

De Vicente, G., Vegas, R., Muñoz-Martín, A., Silva, P.G., Andriessen, P., Cloetingh, S., González-Casado, J.M., Van Wees, J.D., Álvarez, J., Carbó, A., Olaiz, A., 2007. Cenozoic thick-skinned and topography evolution of the Spanish Central System. Glob. Planet. Change 58, 335-381.

De Vicente, G., Vegas, R., 2009. Large-scale distributed deformation controlled topography along the western Africa–Eurasia limit: Tectonic constraints. Tectonophysics 474, 124-143.

De Vicente, G., Vegas, R., Muñoz-Martín, A., Van Wess, J. D., Casas-Sáinz, A., Sopeña, A., Sánchez-Moya, Y., Arche, A., López-Gómez, J., Olaiz, A., Fernández-Lozano, J., 2009. Oblique strain partitioning and transpression on an inverted rift: The Castilian Branch. Tectonophysics 470, 224-242.

Díez, J. B., Broutin, J., Ferrer, J., 2005. Difficulties ecountered in defining the Permian-Triassic boundary in Buntsandstein facies of the western Peritethyan domain based in palynological data. Palaeogeography, Palaeoclimatology, Palaeoecology 229, 40-53.

Dunlop, D.J., 1972. Magnetic mineralogy of unheated and heated red sediments by coercivity spectrum analysis. Geophysical Journal of the Royal Astronomical Society 27, 37-55.

Dunlop, D. J., Özdemir, Ö., 1997. Rock Magnetism. Fundamentals and frontiers. In: Edwards, D., Ed.), Cambridge Studies in Magnetism. Cambridge University Press. 253p.

Frizon de Lamotte, D., Souque, C., Grelaud, S, Robion P., 2002. Erly record of tectonic magnetic fabric durion inversion of a sedimetnary basin. Short review and examples fron the Corbières transfer zone (France). Bulletin de la Société Géologique de France173 (5), 461-469.

García Gil, S., 1989. Estudio sedimentológico y paleogrográfico del Triásico en el tercio noroccidental de la Cordillera Ibérica (provincias de Guadalajara y Soria). Ph.D. Thesis. Universidad Complutense de Madrid. 375p.

García-Lasanta, C., Oliva-Urcia, B., Román-Berdiel, T., Gil-Peña, I., Sánchez-Moya, Y., Sopeña, A., 2013a. Fábricas magnéticas controladas tectónicamente en el Triásico de la Cuenca Ibérica. LIII Sesión Científica, Zaragoza 2012. Geogaceta 53, 53-56.

García-Lasanta, C., Oliva-Urcia, B., Román-Berdiel, T., Casas, A. M., Pérez-Lorente, F., 2013b. Development of magnetic fabric in sedimentary rocks: insights from early compactional structures (ECS). Geophysical Journal International 194 (1), 182-199.

García-Lasanta, C., Oliva-Urcia, B., Román-Berdiel, T., Casas, A. M., Hirt A. M., 2014. Understanding the Mesozoic kinematic evolution in the Cameros basin (Iberian Range, NE Spain) from magnetic subfabrics and mesostructures. Journal of Structural Geology 66, 84-101.

GEODE [online] 2012. Sistema de Información Geológica Continua: SIGECO. IGME. J. Navas (Ed.) [reference date 17/11/2012]. Available in: http://cuarzo.igme.es/sigeco/default.htm

Graham, J. W., 1966. Significance of magnetic anisotropy in Appalachian sedimentary rocks. In: Steinhart, J.S., Smith, T.J., (Eds.) The Earth beneath the continents. American Geophysical Union, Geophysical Monograph Series 627-648.

Guimerà, J., Más, R., Alonso, A., 2004. Intraplate deformation in the NW Iberian Chain: Mesozoic extension and contractional inversion. Journal of the Geological Society of London 16, 291-303.

Hernando, S., 1974. Un depósito tipo raña en la base del Triásico del borde noroccidental de la Cordillera Ibérica (nota previa). Tecniterrae 2, 8-13.

Hernando, S., 1977. Pérmico y Triásico de la región Ayllón-Atienza (provincia de Segovia, Soria y Guadalajara). Editorial de la Universidad Complutense, Madrid. Seminarios de Estratigrafía 2, 1-408.

Hirt, A.M., Almqvist, B.S.G:, 2012. Unraveling magnetic fabrics, International Journal of Earth Sciences 101, 613-624.

Hirt, A. M., Gehring, A. U., 1991. Thermal alteration of the magnetic mineralogy in ferruginous rocks. Journal of Geophysical Research 96 (B6), 9947-9953.

Hrouda, F., 1994. A technique for the measurement of thermal changes of magnetic susceptibility of weakly magnetic rocks by the CS-2 apparatus and KLY-2 Kappabridge. Geophysical Journal International 118, 604-612.

Hrouda, F., Jelinek, V., Zapletal, K., 1997. Refined technique for susceptibility resolution into ferromagnetic and paramagnetic components bases on susceptibility temperature-variations measurement. Geophysica Journal International 129, 715-719.

Ihmlé, P.F., Hirt, A.M., Lowrie, W., Dietrich. D., 1989. Inverse magnetic fabric in deformed limestones of the Morcles Nappe, Switzerland. Geophysical Research Letters 16,1383-1386.

Jelinek, V., 1978. Statistical processing of anisotropy of magnetic susceptibility measured on groups of specimens. Stud. Geoph. Geod. 22, 50-62.

Jelinek, V., 1981. Characterization of the magnetic fabric of rocks. Tectonophysics 79, 63-70.

Kissel, C., Barrier, E., Laj, C., Lee, T., 1986. Magnetic fabric in “undeformed” marine clays from compressional zones. Tectonics 5, 769-781.

Kruiver, P. P., Dekkers, M. J., Heslop, D., 2001. Quantification of magnetic coercivity components by the analysis of acquisition curves of isothermal remanent magnetization. Earth and Planetary Science Letters 189, 269-276.

Lanza, L., Meloni, A., 2006. The Earth's Magnetism: An Introduction for Geologists. Springer 278p.

Larrasoaña, J. C., Pueyo, E. L., Parés, J. M., 2004. An integrated AMS, structural, palaeo- and rock-magnetic study of Eocene marine marls from the Jaca-Pamplona basin (Pyrenees, N Spain); new insights into the timing of magnetic fabric acquisition in weakly deformed mudrocks. In: Martín-Hernández, F., Lüneburg, C.M., Aubourg, C., Jackson, M., (Eds.), Magnetic Fabric: Methods and Applications: Special Publication 238. Geological Society, London, 127-143.

Larrasoaña, J. C., Gómez-Paccard, M., Giralt, S., Roberts, A. P., 2011. Rapid locking of tectonic magnetic fabrics in weakly deformed mudrock. Tectonophysics 507, 16-25.

Lattard, D., Engelmann, R., Kontny, A., Sauerzapf, U., 2006. Curie temperatures of synthetic titanomagnetites in the Fe-Ti-O system: Effects of composition, crystal chemistry, and thermomagnetic methods, Journal of Geophysical Research 111, B12S28, doi:10.1029/2006JB004591.

Liesa, C. L., Simón, J. L., 2009. Evolution of intraplate stress fields under multiple rempote compressions: Te case of the Iberian Chain (NE Spain). Tectonophysics 474, 144-159.

Lowrie, W., Hirt, A. M., 1987. Anisotropy of magnetic susceptibility in the Scaglia Rossa pelagic limestone. Earth and Planetry Science Letters 82, 349-356.

Lowrie, W., 1990. Identification of ferromagnetic minerals in a rock by coercivity and unblocking temperature properties. Geophysical Research Letters 17 (2), 159-162.

Lüneburg, C. M., Lampert, S. A., Hermann, I., Lebit, D., Hirt, A. M., Casey, M., Lowrie, W., 1999. Magnetic anisotropy, rock fabrics and finite strain in deformed sediments of SW Sardinia (Italy). Tectonophysics 307, 51-74.

Martín-Hernández, F., Hirt, A. M., 2001. Separation of ferrimagnetic and paramagnetic anisotropies using a high-field torsion magnetometer. Tectonophysics 337, 209-222.

Martín-Hernández, F., 2002. Determination of fundamental magnetic anisotropy parameters in rock-forming minerals and their contributions to the magnetic fabric of rocks. PhD. Thesis, ETH Zurich, pp.181.

Martín-Hernández, F., Hirt, A. M., 2003. The anisotropy of magnetic susceptibility in biotite, muscovite and chlorite single crystals. Tectonophysics 367, 13-28.

Martín-Hernández, F., Hirt, A. M., 2004. A method for the separation of paramagnetic, ferrimagnetic and haematite magnetic subfabrics using high-field torque magnetometry. Geophysical Journal International 157, 117-127.

Martín-Hernández, F., Ferré, E. C., 2007. Separation of paramagnetic and ferrimagnetic anisotropies: A review. Journal of Gephysical Research 112, B03105, doi:10.1029/2006JB004340.

Martín-Hernández, F., Guerrero-Suárez, S., 2012. Magnetic anisotropy of hematite natural crystals: high field experiments. Int. J. Earth Sci., (Geol Rundsch) 101, 637-647.

Matesanz, J., 1987. Estudio sedimentológico de las facies Buntsandstein en el extremo NW de la Rama Castellana de la Cordillera Ibérica (provincia de Soria). Estudios Geológicos 43, 79-94.

Mattei, M., Sagnotti, L., Faccenna, C., Funiciello, R., 1997. Magnetic fabric of weakly deformed clay-rich sediments in the Italian peninsula: Relationship with compressional and extensional tectonics. Tectonophysics 271, 107-122.

Mattei, M., Speranza, F., Argentieri, A., Rosseti, F., Sagnotti, L., Funiciello, R., 1999. Extensional tectonics in the Amantea basin (Calabria, Italy): a comparison between structural and magnetic anisotropy data. Tectonophysics 307, 33-49.

Moussaid, B., El Ouardi, H., Casas-Sainz, A., Villalaín, J.J., Román-Berdiel, T., Oliva-Urcia, B., Soto, R., Torres-López, S., 2013. Magnetic fabrics in the Jurassic-Cretaceous continental basins of the northern Central High Atlas (Morocco). geodynamic implications. Journal of African Earth Sciences 87, 13-33.

Muñoz, A., Ramos, A., Sopeña, A., Sánchez-Moya, Y., 1995. Caracterización de las unidades litoestratigráficas del Triásico en el subsuelo del tercio noroccidental de la Cordillera Ibérica y áreas adyacentes. Cuadernos de Geología Ibérica 19, 129-171.

Muñoz Recio, A., 1993. Análisis del Pérmico y Triásico en el subsuelo del tercio noroccidental de la Cordillera Ibérica y áreas adyacentes. Ph.D. Thesis. Universidad Complutense de Madrid. 374pp.

Oliva-Urcia, B., Larrasoaña, J. C., Pueyo, E. L., Gil. A., Mata, P., Parés, J. M., Schleicher, A. M., Pueyo, O., 2009. Disentangling magnetic subfabrics and their link to deformation processes in cleaved sedimentary rocks from the Internal Sierras (west central Pyrenees, Spain). Journal of Structural Geology 31 (2), 163-176.

Oliva-Urcia, B., Casas, A. M., Soto, R., Villalaín, J. J. & Kodama, K., 2010a. A transtensional basin model for the Organyà basin (central southern Pyrenees) based on magnetic fabric and brittle structures. Geophysical Journal International 184 (1), 111-130.

Oliva-Urcia, B., Román-Berdiel, T., Casas, A.M., Pueyo, E. L. & Osácar, C., (2010b. Tertiary compressional overprint on Aptian-Albian extensional magnetic fabrics, North-Pyrenean Zone. Journal of Structural Geology 32, 362-376.

Oliva-Urcia, B., Román-Berdiel, T., Casas, A. M., Bógalo, M. F., Osacar, M. C., García-Lasanta, C., 2013. Transition from extensional to compressional magnetic fabrics in the Cretaceous Cabuérniga basin (North Spain). Journal of Structural Geology 46, 220-234.

Parés, J. M., Van Der Pluijm, B. A., Dinarès-Turell, J., 1999. Evolution of magnetic fabrics during incipient deformation of mudrocks (Pyrenees, northern Spain). Tectonophysics, 307, 1-14.

Parés, J. M., Van der Pluijm, B. A., 2002. Phyllosilicate fabric characterization by Low-Temperature Anisotropy of Magnetic Susceptibility (LT-AMS). Geophysical Research Letters 29 (24), 4, doi:10.1029/2002GL015459.

Parés, J. M., 2004. How deformed are weakly deformed mudrocks? Insights from magnetic anisotropy. In: Martín- Hernández, F., Lüneburg, C.M., Aubourg, C., Jackson, M., (Eds.), Magnetic Fabric: Methods and Applications: Special Publication 238. Geological Society, London, 191-203.

Pérez Mazarío, F., Hernando, S., Rincón, R., 1992. Evolución en dos etapas de las cuencas pérmicas del borde Noreste del Sistema Central español. Análisis sedimentológico y procedencia de materiales. Cuadernos de Geología Ibérica 16, 91-114.

Piper, J. D. A., Elliot, M. T., Kneller, B. C., 1996. Anisotropy of magnetic susceptibility in a Palaeozoic flysch basin: the Windermere Supergroup, northern England. Sedimentary Geology 106, 235-258.

Pueyo Anchuela, O., Gil Imaz, A., Pocoví Juan, A., Ipas Lloréns, J. F., 2011. Acquisition and blocking of magnetic fabrics in synsedimentary structures. Eocene Pyrenees, Spain. Geophysical Journal International 186, 1015-1028.

Pueyo Anchuela, O., Ramajo Cordero, J., Gil Imaz, A., Meléndez Hevia, G., 2013. Analysis of anisotropy of magnetic susceptibility in iron-oolitic beds: a potential tool for paleocurrent identification. Int. J. Earth Sci., Geol. Rundsch. 102, 1131-1149.

Ramos, A., Sopeña, A., Sánchez-Moya, Y., Muñoz, A., 1986. Evolution of Buntsandstein fluvial sedimentation in the northwest Iberian ranges, Central Spain. Journal of Sedimentary Petrology 56, 862-875.

Ramos, A., Sopeña, A., Sánchez-Moya, Y., Muñoz, A., 1996. Subsidence analysis, maturity modeling and hydrocarbon generation of the Alpine

sedimentary sequence in the NW of the Iberian Ranges (Central Spain). Cuadernos de Geología Ibérica 21, 23-53.

Razola Mariño, L., 2011. Paleohidráulica de sedimentos fluviales antiguos y sedimentología de los materiales continentales y marinos del Triásico Medio y Superior del NW de la Cordillera Ibérica y su comparación con medios actuales. Editorial de la Universidad Complutense, Madrid, 566pp.

Rees, A. I., 1965. The use of anisotropy of magnetic susceptibility in the estimation of sedimentary fabric. Sedimentology 4, 257-271.

Ritcher, C., Van der Plujim, B. A., 1994. Separation of paramagnetic and ferrimagnetic susceptibilities using low temperature magnetic susceptibilities and comparison with high field methods. Physics of the Earth and Planetary Interiors 82, 113-123.

Robion, P., Grelaud, S., Frizon de Lamotte, D., 2007. Pre-folding magnetic fabrics in fold and thrusts belts: Why the apparent internal deformation of the sedimentary rocks from the Minervois basin (NE-Pyrenees, France) is so high compared to the Potwar basin (SW-Himalaya, Pakistan)? Sedimentary Geology 196, 181-200.

Rochette, P., 1987. Magnetic susceptibility of the rock matrix related to magnetic fabric studies, Journal of Structural Geology 9 (8), 1015-1020.

Sagnotti, L., Speranza, F., Winkler, A., Mattei, M., Funiciello, R., 1998. Magnetic fabric of clay sediments from the external northern Apennines (Italy). Physics of the Earth and Planetary Interiors 105, 73-93.

Sagnotti, L., Winkler, A., Montone, P., Di Bella, L., Florindo, F., Mariucci, M. T., Marra, F., Alfonsi, L., Frepoli, A., 1999. Magnetic anisotropy of Plio-Plesitocene sediments from the Adriatic margin of the northern Apennines (Italy. implications for the time-space evolution of the stress field. Tectonophysics 311, 139-153.

Salas, R., Casas, A., 1993. Mesozoic extensional tectonics, stratigraphy and crustal evolution during the Alpine cycle of the eastern Iberian basin. Tectonophysics 228, 33-55.

Sánchez-Moya, Y., 1992. Evolución sedimentológica y controles estructurales en un borde de cuenca extensional: Comienzo del Mesozoico en un sector del margen occidental de la Cordillera Ibérica. Editorial de la Universidad Complutense, Madrid 232 (92), 414pp.

Sánchez-Moya, Y., Sopeña, A., Muñoz, A., Ramos, A., 1992. Consideraciones teóricas sobre el análisis de la subsidencia. Aplicaciones a un caso real en el borde de la cuenca triásica ibérica. Rev. Soc. Geol. Española 5, 21-40.

Sánchez Moya, Y., Sopeña, A., Ramos, A., 1996. Infill architecture of a non-marine halfgraben Triassic basin (central Spain). Journal of Sedimentary Research 66, 1122-1136.

Sánchez-Moya, Y., Sopeña, A., 2004. 5.3. El Rift Mesozoico Ibérico. In: Geología de España (J.A. Vera, Ed.). SGE-IGME, Madrid. 484-522.

Schmidt, V., Hirt, A. M., Rosselli, P., Martín-Hernández, F., 2007. Separation of diamagnetic and paramagnetic anisotropy by high-field low temperature torque measurements. Geophysical Journal International 168, 40-47.

Simón, J. L., Serón, F., Casas, A. M., 1988. Stress deflection and fracture development in a multidirectional extension regime. Mathematical and experimental approach with field examples. Annales Tectonicae, 2 (1), 21-32.

Sopeña, A., 1979. Estratigrafía del Pérmico y Triásico del Noroeste de la Provincia de Guadalajara. Seminarios de Estratigrafía. Serie Monografías. Editorial de la Universidad Complutense, Madrid 5, 329pp.

Sopeña, A., López, J., Arche, A., Pérez-Arlucea, M., Ramos, A., Virgili, C., Hernando, S., 1988. Permian and Triassic rift basins of the Iberian Peninsula. In: Triassic-Jurassic Rifting.Developments in Geotectonics, 22-B (Manspeizer, W., Ed.), Elsevier, Amsterdam, 757-786.

Sopeña, A., Sánchez-Moya, Y., 1997. Tectonic systems tract and depositional architecture of the western border of the Triassic Iberian Trough (central Spain). Sedimentary Geology 113, 245-267.

Soto, R., Casas-Sainz, A. M., Villalaín, J. J., Oliva-Urcia, B., 2007. Mesozoic extension in the Basque-Cantabrian basin (N Spain. Contributions from AMS and brittle mesostructures. Tectonophysics 445, 373-394.

Soto, R., Casas-Sainz, A. M., Villalaín, J. J., Gil-Imaz, A., Fernández-González, G., Del Río, P., Calvo, M., Mochales, T., 2008. Characterizing the Mesozoic extension direction in the northern Iberian plate margin by anisotropy of magnetic susceptibility (AMS). Journal of Geological Society, London 165, 1007-1018.

Soto, R., Kullberg, J. C., Oliva-Urcia, B, Casas-Sainz, A. M., Villalaín, J. J., 2012. Switch of Mesozoic extensional tectonics style in the Lusitanian basin (Portugal). Insights from magnetic fabrics. Tectonophysics 536-537, 122-135.

Tarling, D. H. and Hrouda, F., 1993. The Magnetic Anisotropy of Rocks. Champman & Hall; 215p.

Van Wees, J.D., Arche, A., Beijdorff, C.G., Lopez-Gomez, J., Cloetingh, S., 1998. Temporal and spatial variations in tectonic subsidence in the Iberian Basin (E Spain). Tectonophysics 300, 285-310.

Vargas, H., Gaspar-Escribano, J. M., López-Gómez, J., Van Wees, J. D., Cloetingh, S., De La Horra. R., Arche, A., 2009. A comparison of the Iberian and Ebro Basins during the Permian and Triassic, eastern Spain: A quantitative subsidence modelling approach. Tectonophysics 474, 160-183.

Winkler, A., Alfonsi, L., Florindo, F., Sagnotti, L., Speranza, F., 1997. The magnetic anisotropy of rocks: principles, techniques and geodynamic applications in the Italian peninsula. Ann. Geof. XL (3), 729-740.

9. Figure captions

Figure 1. Location of the Castilian Branch within the Iberian Range (A) and geological sketch of its westernmost region (B). The structurally differentiated sectors of the basin included in the study are: 1) Retortillo de Soria (RE, 13 sites), 2) Condemios (CO, 3 sites), 3) Alpedroches (AL, 9 sites), 4) Riba de Santiuste (RS, 12 sites), 5) Sigüenza (SI, 7 sites), 6) Romanillos (RO, 4 sites), 7) Yelo (YE, 2 sites) and 8) Arcos de Jalón (AJ, 5 sites) (simplified from GEODE, 2012). C) Cross section restored to the Muschelkalk materials across the RS sector, showing the architecture of the Permo-Triassic rifting, modified from Sánchez-Moya (1992). D) Cross section across the RE sector, modified from Hernando (1974).

Figure 2. A) Detailed cartography of the studied region, including the position of AMS and structural analysis sites. Around the map, diverse stereoplots include structural data (see legend for more information) after restoring bedding to horizontal. Only joints are represented *in situ* using symmetric rose diagrams, but dips in those sites never exceed 15 degrees. Field photographs accompany some stereoplots: B) One pervasive family of joints and a secondary conjugate set in RC19. C) Tension gashes infilled with quartz, with milimetric opening widths in RC13. D) Two normal conjugate faults with several decimeters of displacement in RC7. E) Several pairs of conjugate fault planes in RC5. F) Joints enhanced by erosion in RC17. G) Slickenfibers observed in a fault plane from RC22. H) Set of conjugate normal faults with centimetric displacements in RC24. I) *En échelon* pattern of centimetric tension gashes with around 2mm widths in RC28. J) Two families of oblique tension gashes in RC33.

Figure 3. Several cross sections showing the present main shape of the Triassic materials in the Castilian Brach. See fig. 2A for cross sections location and sedimentary legend.

Figure 4. Frequency histogram for the whole bulk susceptibility values (k_m).

Figure 5. Temperature-dependent susceptibility curves obtained for 5 representative samples. Black curves indicate heating and grey curves cooling.

Figure 6. A) IRM acquisition curves from samples RO4-1A and SI6-13A. B) Coercivity component analysis of the IRM acquisition curves. For each component, the value of the mean coercivity and the percentage of relative contribution to the IRM are shown. C) Stepwise thermal demagnetization of the composite IRM.

Figure 7. Average AMS parameters with their error bars from sites taken in Permian (crosses), Buntsandstein (diamonds), Muschelkalk (squares) and Keuper (triangles) facies. A) Corrected anisotropy degree (Pj) versus bulk magnetic susceptibility (k_m). B) Pj versus shape parameter (T).

Figure 8. Equal area projection of the three magnetic axes after restoring bedding to horizontal, for eight representative sites (see text for further information). k_{max} in squares, k_{int} in triangles and k_{min} in circles.

Figure 9. Above, a detailed geological map of the study area is represented (modified from GEODE, 2012), where the eight different sectors are numbered as in Fig. 1. Consecutive figures show each specific area and include the orientation of the magnetic lineation of each site, after restoring bedding to horizontal and superimposed to the geological map. Sites with a magnetic lineation showing a radial distribution are represented with a white circle. White lines are used for magnetic lineations interpreted to be extension-related. Black lines represent magnetic lineations for sites where k_{min} and k_{int} are distributed in a girdle, and therefore, interpreted to be affected by later compressional stage, and grey lines represent magnetic lineations in sites where an incipient girdle was recognized and can be interpreted as transitional between extension and compression-related. For each sector, a plot with magnetic lineations from all samples were represented after restoring bedding to horizontal, including a density stereoplot (contour interval: 1%) and a symmetric rose diagram (bin size: 10 degrees, value of perimeter 30%).

Figure 10. Results, *in situ* and in equal area projection, of low-field AMS at room temperature (black symbols) and low-field AMS at low temperature (white symbols) for three sites representative in the study of subfabrics separation. k_{max} in squares, k_{int} in triangles and k_{min} in circles. Dashed grey line represents bedding plane for each case.

Figure 11. Stereoplot, *in situ* equal area projection, of high-field AMS results (dark grey for the not-saturated fraction and pale grey for the saturated fraction) compared to low-field AMS results at room temperature (black symbols). k_{max} in squares, k_{int} in triangles and k_{min} in circles. Dashed grey line represents bedding plane for each case.

Figure 12. Equal area projection of magnetic lineations (k_{max}) measured at low-field AMS at room temperature of samples in A) Permian and Buntsandstein, B) Muschelkalk and C) Keuper materials, from sites considered as extension-related. Data were plotted after restoring bedding to horizontal, including a density stereoplot (contour interval: 1%) and a symmetric rose diagram (bin size: 5 degrees, value of perimeter 10%).

Figure 13. Sketch of the tectonic frame during the Permian-Triassic Iberian Rift. Grey arrows show the main extension direction. Black arrows show the variations of the extension direction along the rift due to strain partitioning processes.

10. Table captions

Table 1. Summary of magnetic scalar data.

Site: Name of site (sites are ordered consecutively by sectors as numbered in Fig. 1); UTM: UTM coordinates (all sites are located in Time Zone 30T, Datum: ETRS89); N: number of specimens; km: bulk susceptibility (in SI units); Age: geological age of each unit (PB: Permian or Early Triassic-Buntsandstein facies, M: Middle Triassic-Muschelkalk facies, K: Late Triassic, Keuper facies); Pj: corrected anisotropy degree; T: shape parameter; L: magnetic lineation; F: magnetic foliation; e: standard deviation.

Table 2. Summary of magnetic directional data.

In situ values for k_{max}, k_{int} and k_{min} mean orientations (T/P: trend/plunge) from the 55 sites of the study; Conf Ang: confidence angles (major and minor semi-axes for the confidence ellipse with the 95% probability), based on Jelinek statistics (Jelinek, 1978) and calculated with Anisoft42 (Chadima and Jelinek, 2009). S_0: Strike and dip of the bedding planes following the right-hand-rule system.

Table 3. Summary of bulk susceptibility data and magnetic directional data from specimens measured both at room and at low temperature.

RT: room temperature; LT, low temperature; *km*: bulk susceptibility (in SI units); *in situ* values for k_{max}, k_{int} and k_{min} mean orientations (T/P: trend/plunge); Conf Ang: confidence angles (major and minor semi-axes for the confidence ellipse with the 95% probability), based on Jelinek statistics (Jelinek, 1978) and calculated with Anisoft42 (Chadima and Jelinek, 2009). S_0: Strike and dip of the bedding planes following the right-hand-rule system.

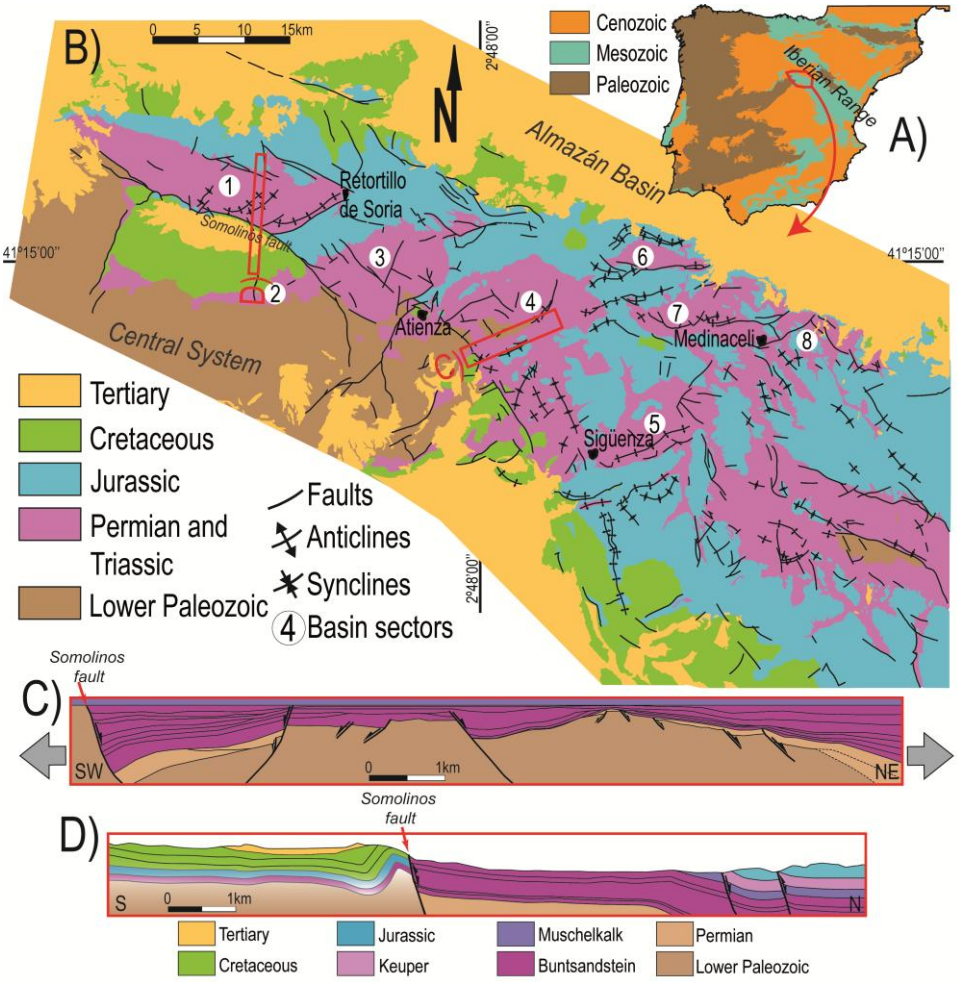

Figure 1. Location of the Castilian Branch within the Iberian Range (A) and geological sketch of its westernmost region (B). The structurally differentiated sectors of the basin included in the study are: 1) Retortillo de Soria (RE, 13 sites), 2) Condemios (CO, 3 sites), 3) Alpedroches (AL, 9 sites), 4) Riba de Santiuste (RS, 12 sites), 5) Sigüenza (SI, 7 sites), 6) Romanillos (RO, 4 sites), 7) Yelo (YE, 2 sites) and 8) Arcos de Jalón (AJ, 5 sites) (simplified from GEODE, 2012). C) Cross section restored to the Muschelkalk materials across the RS sector, showing the architecture of the Permo-Triassic rifting, modified from Sánchez-Moya (1992). D) Cross section across the RE sector, modified from Hernando (1974).

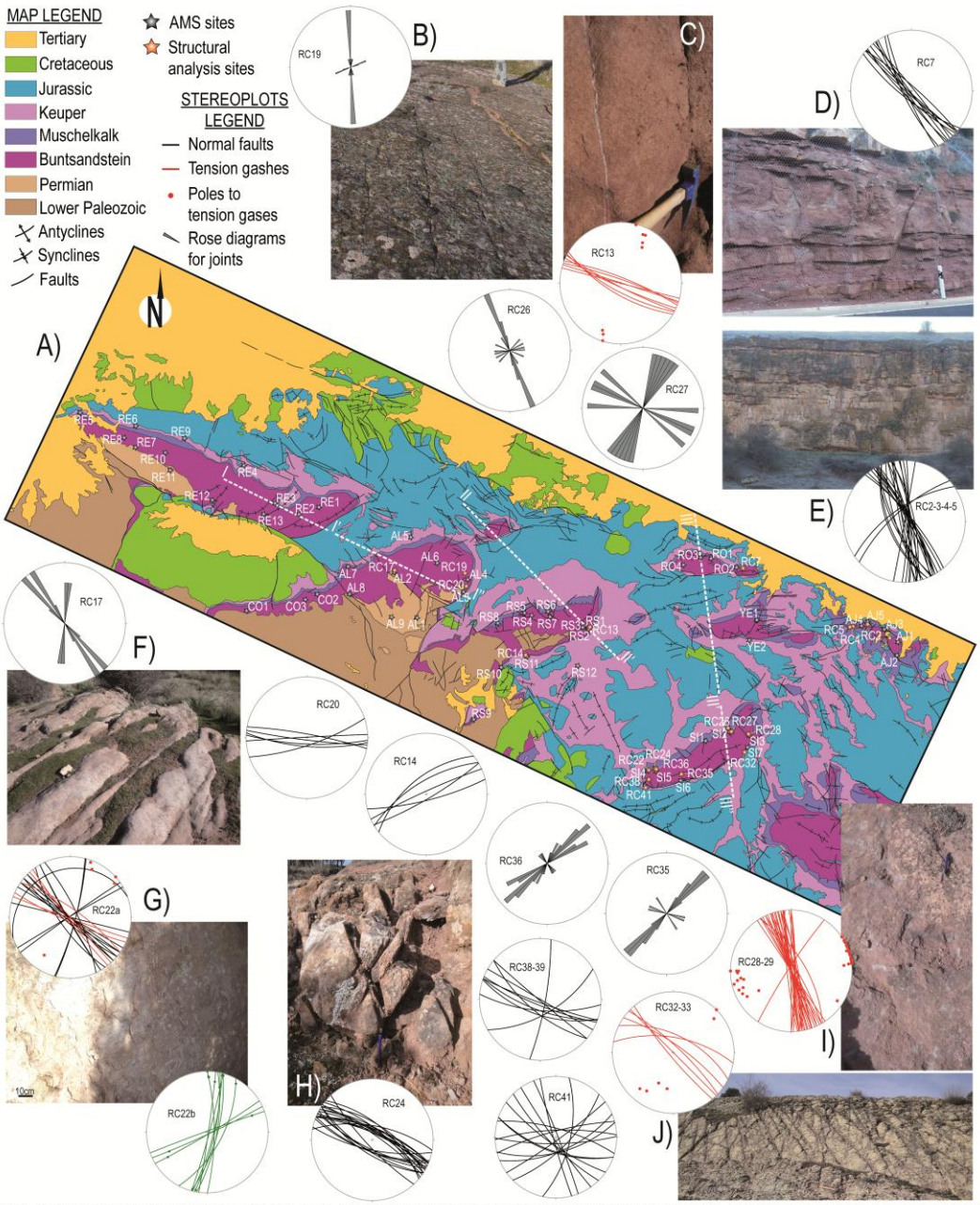

Figure 2. A) Detailed cartography of the studied region, including the position of AMS and structural analysis sites. Around the map, diverse stereoplots include structural data (see legend for more information) after restoring bedding to horizontal. Only joints are represented in situ using symmetric rose diagrams, but dips in those sites never exceed 15 degrees. Field photographs accompany some stereoplots: B) One pervasive family of joints and a secondary conjugate set in RC19. C) Tension gashes infilled with quartz, with milimetric opening widths in RC13. D) Two normal conjugate faults with several decimeters of displacement in RC7. E) Several pairs of conjugate fault planes in RC5. F) Joints enhanced by erosion in RC17. G) Slickenfibers observed in a fault plane from RC22. H) Set of conjugate normal faults with centimetric displacements in RC24. I) En échelon pattern of centimetric tension gashes with around 2mm widths in RC28. J) Two families of oblique tension gashes in RC33.

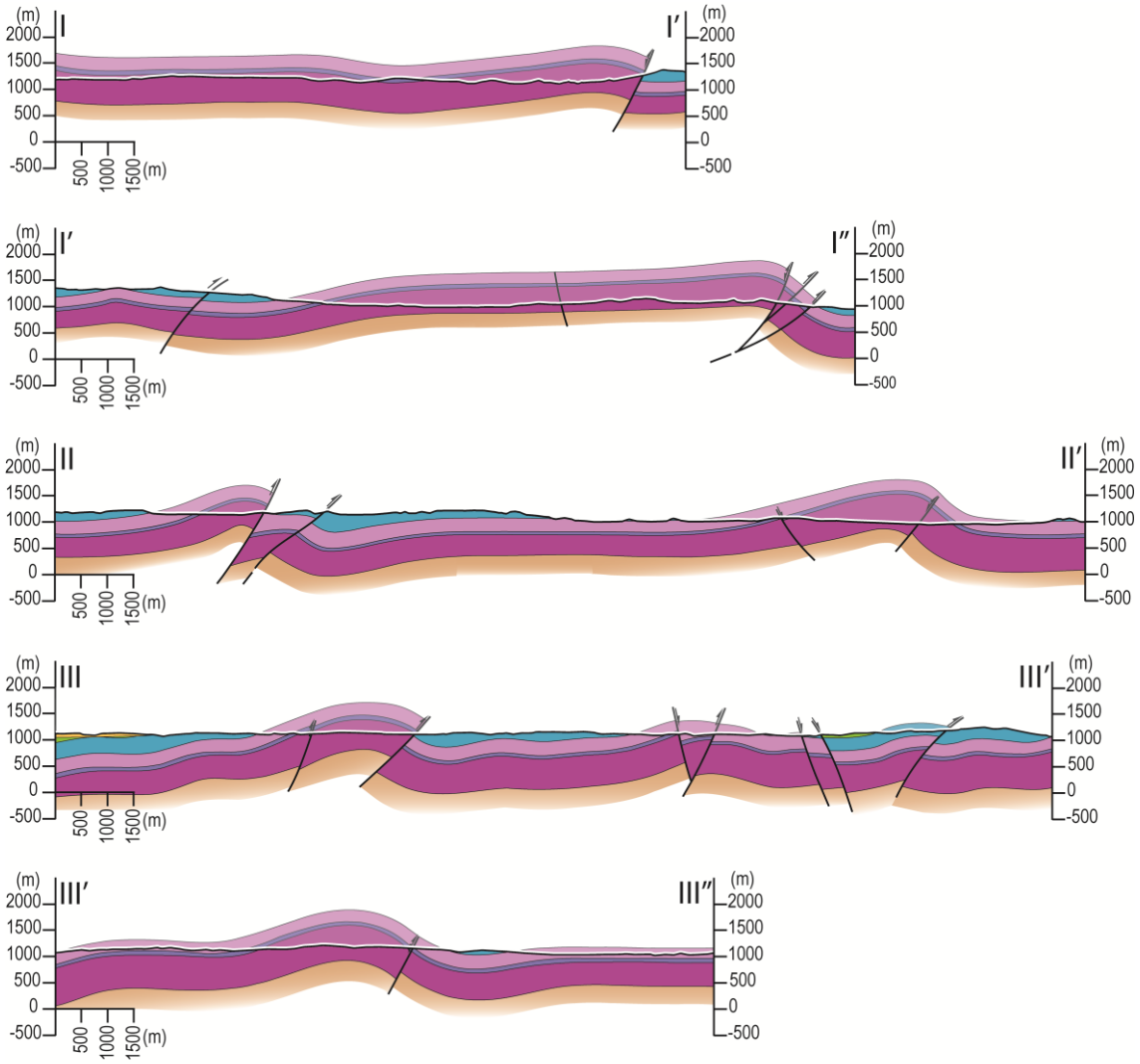

Figure 3. Several cross sections showing the present main shape of the Triassic materials in the Castilian Brach. See fig. 2A for cross sections location and sedimentary legend.

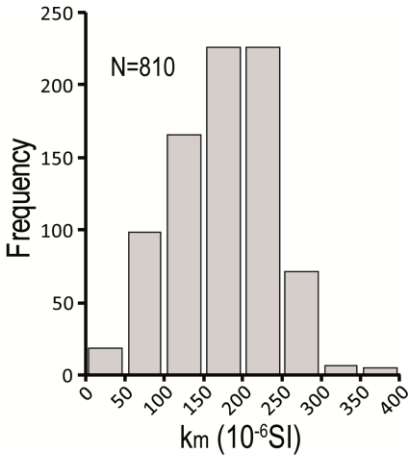

Figure 4. Frequency histogram for the whole bulk susceptibility values (k_m).

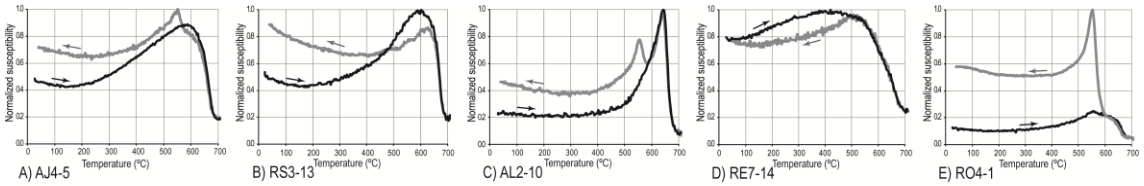

Figure 5. Temperature-dependent susceptibility curves obtained for 5 representative samples. Black curves indicate heating and grey curves cooling.

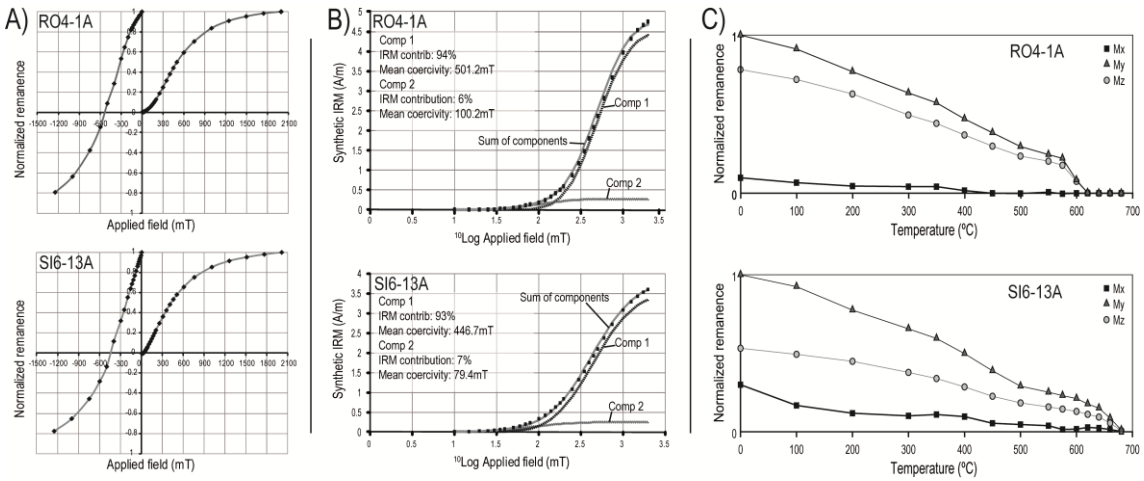

Figure 6. A) IRM acquisition curves from samples RO4-1A and SI6-13A. B) Coercivity component analysis of the IRM acquisition curves. For each component, the value of the mean coercivity and the percentage of relative contribution to the IRM are shown. C) Stepwise thermal demagnetization of the composite IRM.

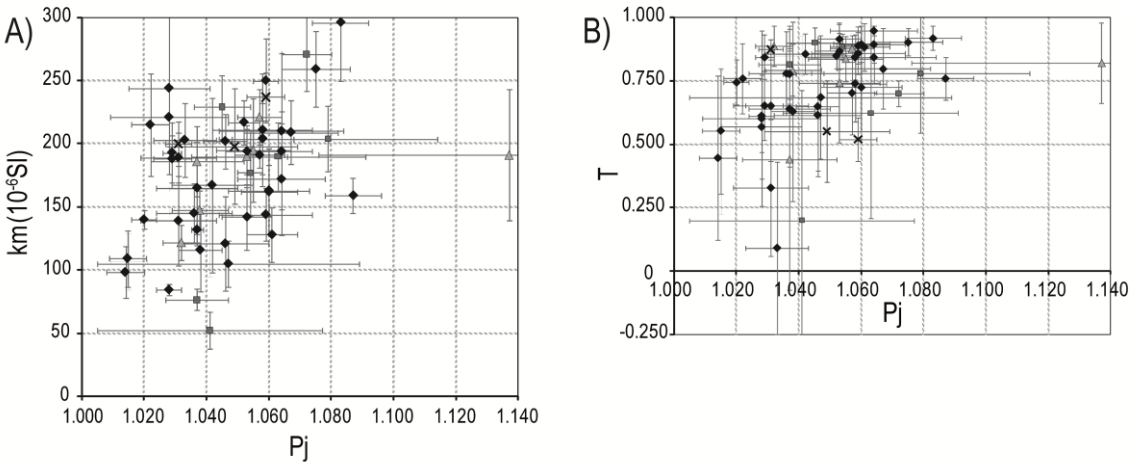

Figure 7. Average AMS parameters with their error bars from sites taken in Permian (crosses), Buntsandstein (diamonds), Muschelkalk (squares) and Keuper (triangles) facies. A) Corrected anisotropy degree (Pj) versus bulk magnetic susceptibility (km). B) Pj versus shape parameter (T).

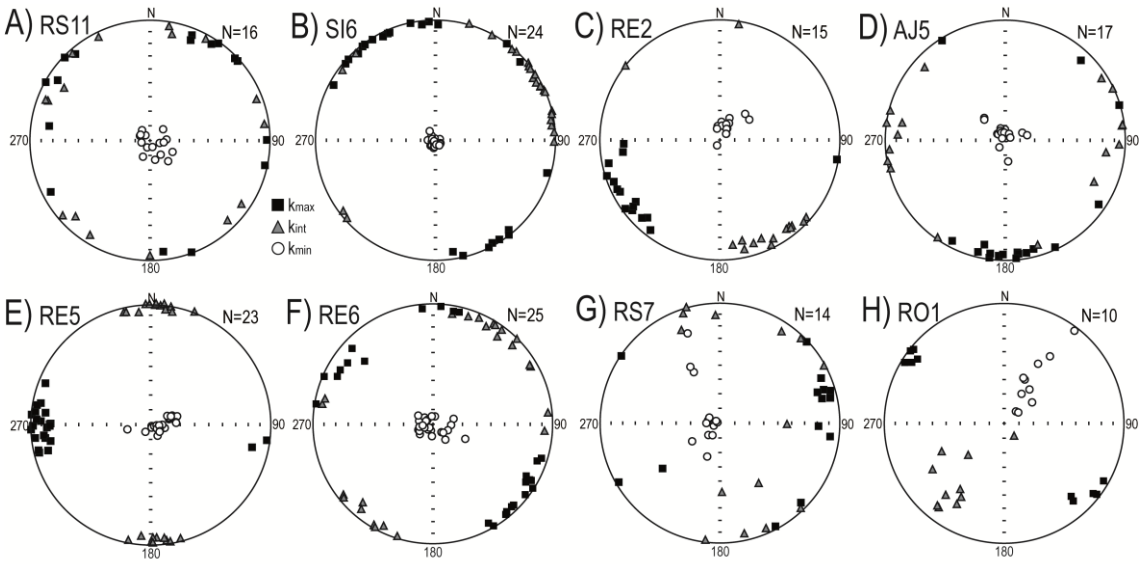

Figure 8. Equal area projection of the three magnetic axes after restoring bedding to horizontal, for eight representative sites (see text for further information). k_{max} in squares, k_{int} in triangles and k_{min} in circles.

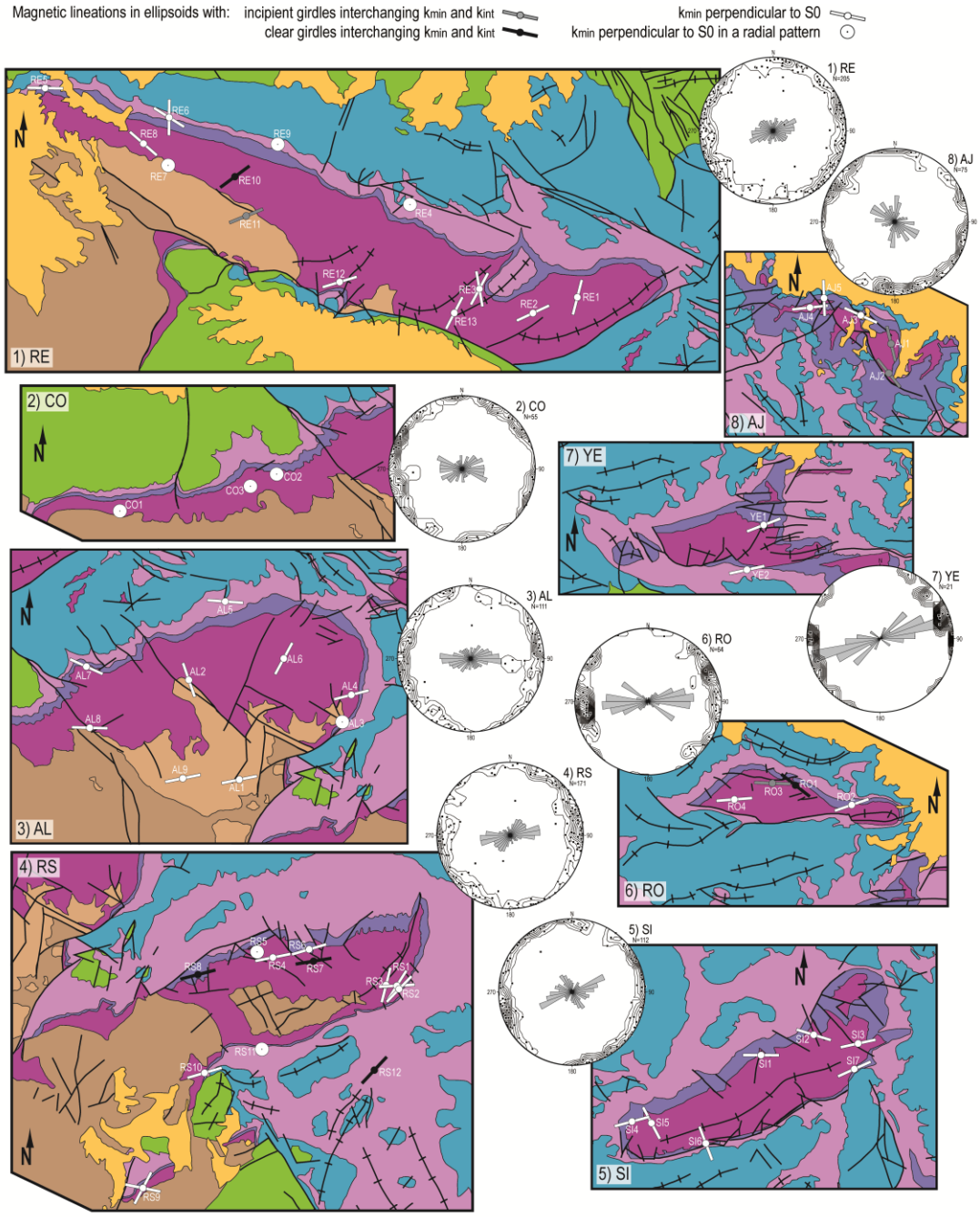

Figure 9. Above, a detailed geological map of the study area is represented (modified from GEODE, 2012), where the eight different sectors are numbered as in Fig. 1. Consecutive figures show each specific area and include the orientation of the magnetic lineation of each site, after restoring bedding to horizontal and superimposed to the geological map. Sites with a magnetic lineation showing a radial distribution are represented with a white circle. White lines are used for magnetic lineations interpreted to be extension-related. Black lines represent magnetic lineations for sites where kmin and kint are distributed in a girdle, and therefore, interpreted to be affected by later compressional stage, and grey lines represent magnetic lineations in sites where an incipient girdle was recognized and can be interpreted as transitional between extension and compression-related. For each sector, a plot with magnetic lineations from all samples were represented after restoring bedding to horizontal, including a density stereoplot (contour interval: 1%) and a symmetric rose diagram (bin size: 10 degrees, value of perimeter 30%).

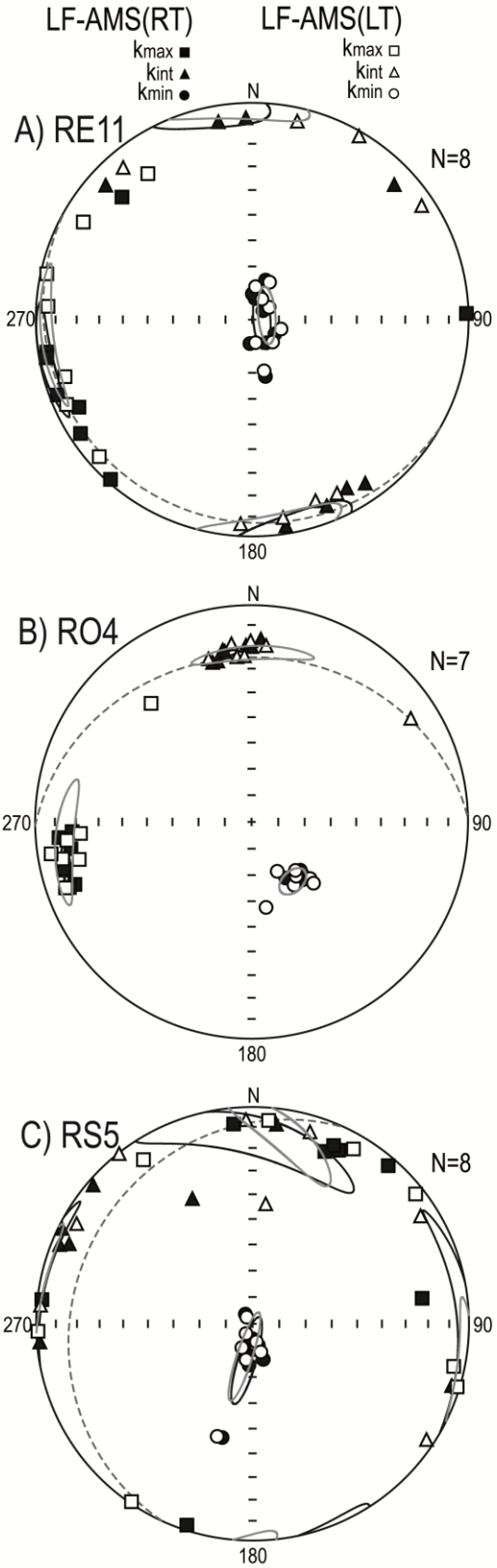

Figure 10. Results, in situ and in equal area projection, of low-field AMS at room temperature (black symbols) and low-field AMS at low temperature (white symbols) for three sites representative in the study of subfabrics separation. k_{max} in squares, k_{int} in triangles and k_{min} in circles. Dashed grey line represents bedding plane for each case.

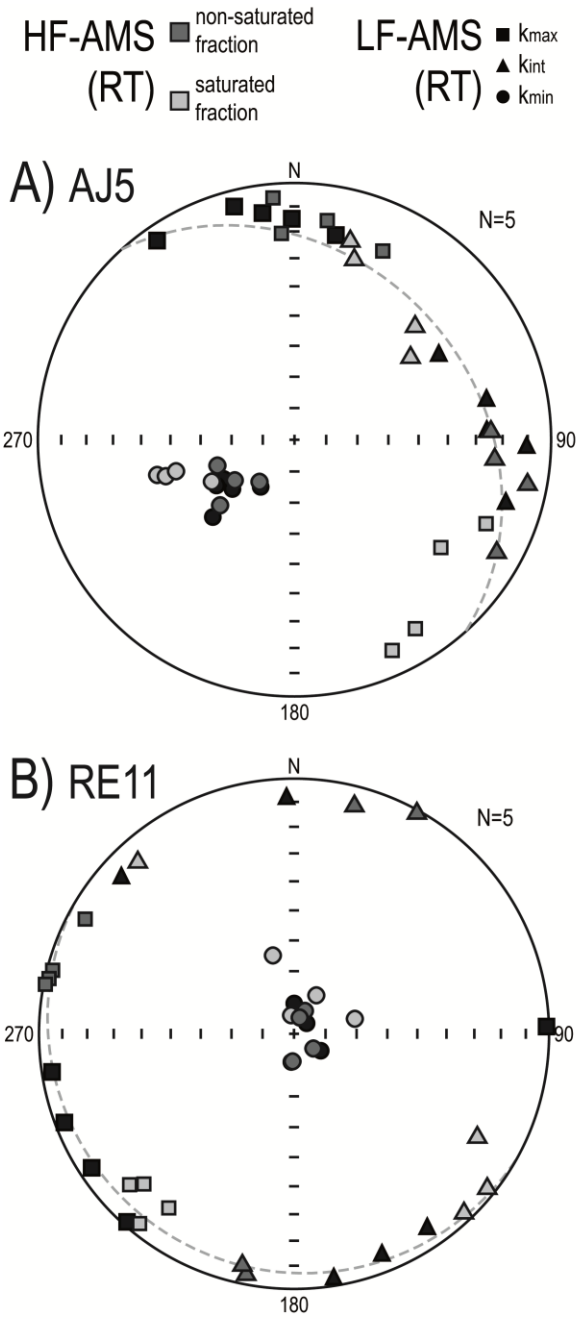

Figure 11. Stereoplot, in situ equal area projection, of high-field AMS results (dark grey for the not-saturated fraction and pale grey for the saturated fraction) compared to low-field AMS results at room temperature (black symbols). k_{max} in squares, k_{int} in triangles and k_{min} in circles. Dashed grey line represents bedding plane for each case.

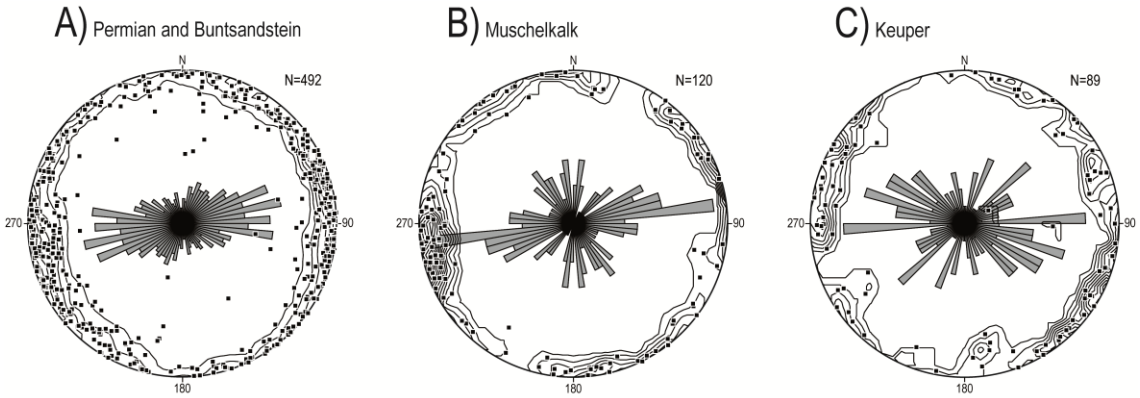

Figure 12. Equal area projection of magnetic lineations (kmax) measured at low-field AMS at room temperature of samples in A) Permian and Buntsandstein, B) Muschelkalk and C) Keuper materials, from sites considered as extension-related. Data were plotted after restoring bedding to horizontal, including a density stereoplot (contour interval: 1%) and a symmetric rose diagram (bin size: 5 degrees, value of perimeter 10%).

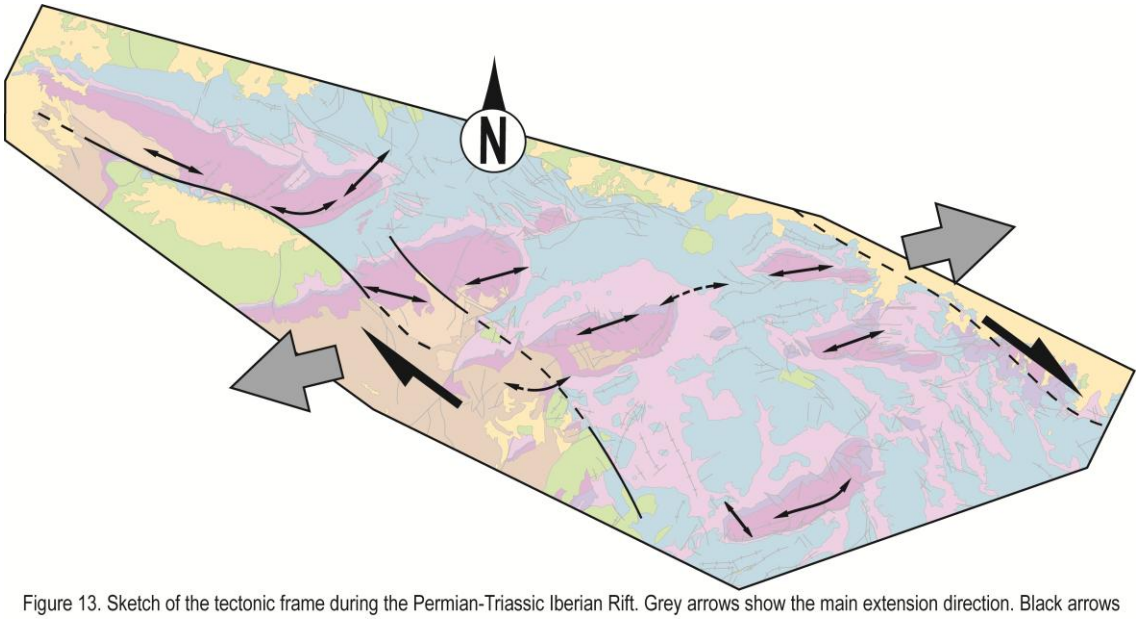

Figure 13. Sketch of the tectonic frame during the Permian-Triassic Iberian Rift. Grey arrows show the main extension direction. Black arrows show the variations of the extension direction along the rift due to strain partitioning processes.

Site	UTM East	UTM North	N	Age	km ($x10^{-6}$ SI)	e ($x10^{-6}$ SI)	L	e	F	e	Pj	e	T	e
RE1	497245.21	4572903.24	11	PB	189.0	19.8	1.011	0.008	1.019	0.007	1.031	0.012	0.328	0.270
RE2	495236.57	4572208.1	15	PB	140.0	7.39	1.002	0.001	1.016	0.003	1.020	0.004	0.745	0.088
RE3	492801.79	4573282.63	13	PB	139.0	35.2	1.005	0.003	1.024	0.010	1.031	0.012	0.652	0.219
RE4	489744.76	4577173.86	9	K	147.0	15.8	1.004	0.003	1.030	0.007	1.038	0.009	0.786	0.107
RE5	474382.49	4582469.66	23	M	271.0	29.3	1.010	0.002	1.056	0.007	1.072	0.008	0.701	0.050
RE6	479529.27	4581140.28	25	K	191.0	52.0	1.008	0.005	1.113	0.052	1.137	0.061	0.821	0.160
RE7	479130.91	4578838.57	15	PB	215.0	40.5	1.002	0.002	1.018	0.005	1.022	0.006	0.760	0.138
RE8	478336.15	4579959.74	19	PB	217.0	17.6	1.003	0.001	1.043	0.005	1.052	0.005	0.850	0.050
RE9	483799.54	4579921.16	14	K	122.0	14.0	1.002	0.001	1.026	0.004	1.032	0.006	0.888	0.080
RE10	482061.66	4578406.53	12	PB	105.0	18.2	1.010	0.016	1.034	0.026	1.047	0.042	0.686	0.244
RE11	482499.5	4576651.95	17	PB	200.0	17.8	1.002	0.001	1.026	0.003	1.031	0.004	0.874	0.041
RE12	486546.08	4573555.85	18	PB	193.0	24.0	1.002	0.001	1.024	0.003	1.029	0.003	0.844	0.087
RE13	491704.84	4572192.96	12	PB	221.0	23.5	1.004	0.003	1.021	0.017	1.028	0.019	0.602	0.346
CO1	489943.69	4562506.26	8	PB	250.0	33.2	1.003	0.002	1.050	0.003	1.059	0.004	0.890	0.073
CO2	496984.55	4564247.19	12	PB	296.0	46.3	1.003	0.002	1.070	0.008	1.083	0.009	0.919	0.048
CO3	495837.85	4563607.99	34	PB	167.0	68.0	1.003	0.001	1.034	0.011	1.042	0.013	0.854	0.077

AL1	507053.14	4561798.13	9	PB	198.0	45.8	1.009	0.002	1.037	0.018	1.049	0.02	0.551	0.201
AL2	504679.28	4566378.77	15	PB	98.3	20.5	1.004	0.003	1.010	0.005	1.014	0.006	0.446	0.323
AL3	511710.04	4564413.84	16	PB	194.0	31.4	1.003	0.002	1.054	0.009	1.064	0.01	0.895	0.073
AL4	512069.85	4565664.90	13	PB	202.0	21.6	1.008	0.006	1.035	0.007	1.046	0.007	0.650	0.253
AL5	506422.78	4569858.97	12	K	221.0	21.9	1.003	0.001	1.048	0.006	1.057	0.007	0.878	0.052
AL6	509114.68	4567306.72	12	PB	159.0	14.2	1.009	0.003	1.069	0.008	1.087	0.009	0.760	0.084
AL7	500142.59	4566948.77	9	M	204.0	26.0	1.005	0.004	1.065	0.032	1.079	0.035	0.781	0.236
AL8	500161.25	4564040.09	13	PB	188.0	18.7	1.004	0.002	1.022	0.005	1.029	0.006	0.653	0.138
AL9	504521.57	4561823.54	12	PB	237.0	19.0	1.013	0.002	1.042	0.005	1.059	0.006	0.519	0.086
RS1	524452.62	4560559.98	16	PB	165.0	36.4	1.006	0.003	1.028	0.011	1.037	0.013	0.640	0.228
RS2	524456.98	4560581.22	10	PB	204.0	28.1	1.006	0.004	1.046	0.010	1.058	0.010	0.740	0.152
RS3	523833.05	4560696.69	16	PB	209.0	25.4	1.006	0.005	1.054	0.013	1.067	0.015	0.798	0.159
RS4	518728.81	4561982.52	14	PB	163.0	20.1	1.007	0.005	1.047	0.011	1.060	0.013	0.725	0.175
RS5	517966.71	4562226.69	21	PB	144.0	20.7	1.004	0.003	1.049	0.012	1.059	0.015	0.860	0.082
RS6	520290.05	4562308.64	14	M	229.0	25.4	1.002	0.001	1.037	0.007	1.045	0.009	0.899	0.060
RS7	520447.77	4561868.72	14	PB	128.0	21.4	1.003	0.003	1.051	0.007	1.061	0.008	0.884	0.093
RS8	515261.06	4561197.34	12	M	190.0	27.0	1.008	0.008	1.049	0.027	1.063	0.028	0.623	0.415
RS9	512802.03	4551382.76	13	PB	109.0	22.5	1.003	0.002	1.011	0.005	1.015	0.006	0.550	0.243
RS10	515586.49	4556687.18	17	PB	244.0	68.0	1.005	0.002	1.021	0.011	1.028	0.013	0.569	0.206

RS11	518198.45	4557821.85	16	K	190.0	24.5	1.006	0.006	1.042	0.012	1.053	0.013	0.743	0.237
RS12	523380.07	4556826.38	7	K	186.0	27.9	1.008	0.004	1.027	0.015	1.037	0.015	0.440	0.516
SI1	536341.50	4549359.62	9	PB	172.0	44.3	1.001	0.000	1.055	0.012	1.064	0.014	0.949	0.020
SI2	538764.68	4550310.91	9	PB	162.0	34.0	1.003	0.002	1.050	0.008	1.060	0.009	0.896	0.071
SI3	540806.74	4549889.27	10	PB	191.0	10.2	1.007	0.003	1.045	0.009	1.057	0.008	0.703	0.164
SI4	530524.17	4546296.73	12	PB	145.0	23.4	1.004	0.004	1.029	0.009	1.036	0.012	0.780	0.165
SI5	531279.52	4546250.07	15	PB	116.0	32.7	1.007	0.007	1.029	0.008	1.038	0.007	0.630	0.354
SI6	533886.17	4545327.48	24	M	76.6	8.38	1.003	0.004	1.030	0.007	1.037	0.010	0.814	0.155
SI7	540603.98	4548821.73	33	M	52.1	14.6	1.011	0.005	1.028	0.032	1.041	0.036	0.200	0.513
RO1	536855.86	4567767.16	10	PB	203.0	29.0	1.013	0.003	1.019	0.009	1.033	0.010	0.090	0.340
RO2	539361.04	4566921.74	24	PB	211.0	44.3	1.004	0.002	1.048	0.014	1.058	0.016	0.844	0.089
RO3	535784.24	4567917.23	9	PB	121.0	37.3	1.008	0.005	1.035	0.012	1.046	0.014	0.616	0.242
RO4	534058.21	4567100.38	21	PB	84.4	4.42	1.005	0.002	1.022	0.004	1.028	0.004	0.613	0.145
YE1	541552.1	4561506.98	8	PB	132.0	12.1	1.004	0.002	1.030	0.002	1.037	0.002	0.778	0.100
YE2	540805.78	4559526.66	13	K	195.0	40.9	1.004	0.003	1.045	0.009	1.055	0.012	0.837	0.088
AJ1	555846.47	4558097.78	14	PB	194.0	17.8	1.002	0.001	1.045	0.006	1.053	0.007	0.916	0.059
AJ2	555932.51	4559163.75	14	PB	142.0	25.9	1.003	0.002	1.044	0.007	1.053	0.008	0.868	0.072
AJ3	554292.66	4560741.19	17	PB	210.0	61.8	1.004	0.003	1.053	0.017	1.064	0.020	0.844	0.106
AJ4	552182.01	4561010.96	13	PB	259.0	30.1	1.003	0.002	1.063	0.009	1.075	0.011	0.903	0.054

AJ5	552736.64	4561381.67	17	M	177.0	34.3	1.003	0.001	1.045	0.003	1.054	0.004	0.884	0.051

Table 1. Summary of magnetic scalar data.

Site: Name of site (sites are ordered consecutively by sectors as numbered in Fig. 1); UTM: UTM coordinates (all sites are located in Time Zone 30T, Datum: ETRS89); N: number of specimens; km: bulk susceptibility (in SI units); Age: geological age of each unit (PB: Late Permian or Early Triassic-Buntsandstein facies, M: Middle Triassic-Muschelkalk facies, K: Late Triassic, Keuper facies); Pj: corrected anisotropy degree; T: shape parameter; L: magnetic lineation; F: magnetic foliation; e: standard deviation.

Site	k_{max} (T/P)	Conf Ang (º)	k_{int} (T/P)	Conf Ang (º)	k_{min} (T/P)	Conf Ang (º)	S_0
RE1	11/4	19/10	279/18	16/13	113/72	17/13	260/14
RE2	245/1	24/6	335/3	24/4	137/87	6/4	282/11
RE3	358/6	22/6	90/18	24/17	252/71	20/6	000/00
RE4	287/6	11/5	196/8	16/10	53/80	16/4	269/05
RE5	270/8	10/6	3/22	9/4	160/67	8/3	269/22
RE6	310/9	31/6	42/14	31/5	189/74	7/4	269/15
RE7	321/8	52/5	52/8	52/14	188/79	16/3	000/00
RE8	301/5	34/8	32/21	34/4	199/68	9/4	269/20
RE9	320/9	69/4	52/7	69/10	179/78	10/4	265/25
RE10	56/5	21/14	147/16	45/18	310/73	45/13	281/21
RE11	255/4	14/3	165/2	14/9	48/86	10/3	120/08
RE12	260/1	29/10	170/18	29/6	354/72	11/4	080/17
RE13	22/2	26/8	292/1	26/4	190/88	10/4	110/08
CO1	3/3	49/5	273/2	49/4	147/87	7/5	000/00
CO2	33/4	81/3	303/4	81/5	166/84	5/4	186/07
CO3	305/7	68/5	215/3	68/9	105/82	13/5	269/02
AL1	255/12	21/8	165/4	19/4	58/78	12/4	167/09
AL2	344/11	24/9	252/13	24/15	114/73	16/10	269/05
AL3	90/41	35/9	208/29	35/14	321/36	14/10	061/56
AL4	78/14	31/12	346/9	32/5	255/73	13/8	005/13
AL5	303/15	30/6	37/14	31/14	168/69	16/5	269/02
AL6	215/2	21/9	125/2	21/11	355/87	13/5	277/06

AL7	298/5	29/11	30/18	29/11	192/71	12/11	303/10
AL8	274/8	44/9	5/8	44/8	139/78	11/11	190/10
AL9	81/13	21/6	350/6	19/5	237/76	11/6	269/02
RS1	73/44	37/11	203/34	37/12	313/27	14/8	046/55
RS2	234/2	24/6	139/65	23/3	325/25	7/3	046/55
RS3	207/12	55/11	106/44	55/8	308/44	13/5	038/55
RS4	256/7	17/6	347/14	17/5	140/74	6/5	210/12
RS5	280/3	39/6	11/9	39/14	172/80	14/6	205/18
RS6	245/0	27/4	155/3	27/8	338/87	9/4	240/10
RS7	254/14	12/4	346/8	23/8	104/74	22/5	197/26
RS8	76/0	18/6	346/11	18/10	167/79	11/7	230/10
RS9	268/9	59/11	359/10	59/8	139/77	12/9	300/10
RS10	66/28	45/10	166/19	45/10	286/55	13/5	020/38
RS11	102/46	37/8	247/38	37/6	352/18	8/6	080/75
RS12	53/16	26/10	144/4	28/26	246/74	28/10	000/00
SI1	90/2	19/3	359/10	22/7	191/80	14/2	255/11
SI2	289/2	28/9	199/1	28/4	85/88	9/4	000/00
SI3	249/6	16/3	158/17	16/3	358/72	4/3	083/16
SI4	256/3	32/14	347/15	32/10	153/75	15/10	176/06
SI5	337/7	25/7	246/2	25/8	138/83	9/6	219/13
SI6	148/27	25/3	245/13	25/2	358/59	3/2	090/32
SI7	62/9	16/4	157/25	16/5	313/63	7/5	048/40
RO1	307/2	8/4	216/26	16/6	41/64	16/4	265/05
RO2	68/4	24/4	336/25	24/3	167/64	4/3	235/25
RO3	89/7	16/4	356/26	21/5	193/63	15/5	000/00
RO	256/12	8/2	351/23	9/3	141/64	3/2	269/25

4							
YE1	71/4	27/5	340/4	27/3	205/85	6/4	335/08
YE2	255/11	24/10	157/34	24/6	000/54	11/5	090/55
AJ1	129/4	37/4	39/1	37/9	293/86	11/3	176/05
AJ2	310/1	28/5	41/18	29/11	217/72	13/6	320/40
AJ3	116/1	17/4	26/6	17/4	214/84	5/4	000/00
AJ4	93/3	36/6	3/3	36/4	232/86	8/4	000/00
AJ5	358/16	30/6	95/23	30/7	236/62	8/5	318/30

Table 2. Summary of magnetic directional data.

In situ values for k_{max}, k_{int} and k_{min} mean orientations (T/P: trend/plunge) from the 55 sites of the study; Conf Ang: confidence angles (major and minor semi-axes for the confidence ellipse with the 95% probability), based on Jelinek statistics (Jelinek, 1978) and calculated with Anisoft42 (Chadima and Jelinek, 2009). S_0: Strike and dip of the bedding planes following the right-hand-rule system.

ite	km ($x10^{-6}$)	e ($x10^{-6}$)	k_{max} (T/P)	Conf Ang (º)	k_{int} (T/P)	Conf Ang (º)	k_{min} (T/P)	Conf Ang (º)	LT/RT
L5RT	235	15.3	309/17	20/4	42/12	26/15	165/70	23/2	2.71
L5LT	638	27.8	314/17	11/2	47/10	24/7	166/70	22/1	
E11RT	207	14.2	258/4	16/3	348/1	384/1	86/86	11/3	2.10
E11LT	434	18.7	265/6	20/3	175/1	21/9	74/84	11/3	
O4RT	84.9	4.97	256/13	7/2	352/23	7/1	139/63	3/1	2.30
O4LT	195	20.3	264/14	19/4	0/23	19/3	145/63	6/4	
S5RT	148	19.7	91/2	35/4	0/14	36/9	189/76	17/3	2.21
S5LT	327	51.7	100/1	18/3	10/13	23/6	194/77	18/3	
I5RT	145	28.4	333/4	24/8	243/2	25/5	132/85	11/7	2.47
I5LT	358	88.7	254/3	28/4	344/3	29/7	122/86	11/3	

Table 3. Summary of bulk susceptibility data and magnetic directional data from specimens measured both at room and at low temperature.

RT: room temperature; LT, low temperature; *km*: bulk susceptibility (in SI units); *in situ* values for k_{max}, k_{int} and k_{min} mean orientations (T/P: trend/plunge); Conf Ang: confidence angles (major and minor semi-axes for the confidence ellipse with the 95% probability), based on Jelinek statistics (Jelinek, 1978) and calculated with Anisoft42 (Chadima and Jelinek, 2009). S_0: Strike and dip of the bedding planes following the right-hand-rule system.

Highlights

- Magnetic fabrics used to unravel the deformational history of an inverted basin.

- Hematite (main) and phyllosilicates are the main contributors to the AMS.

- k_{min} axes usually perpendicular to bedding, according to a sedimentary fabric.

- k_{max} orientations (ENE-WSW) fit with a dextral transtensional regime.

- Strain partitioning inferred from variations in magnetic lineation orientations.